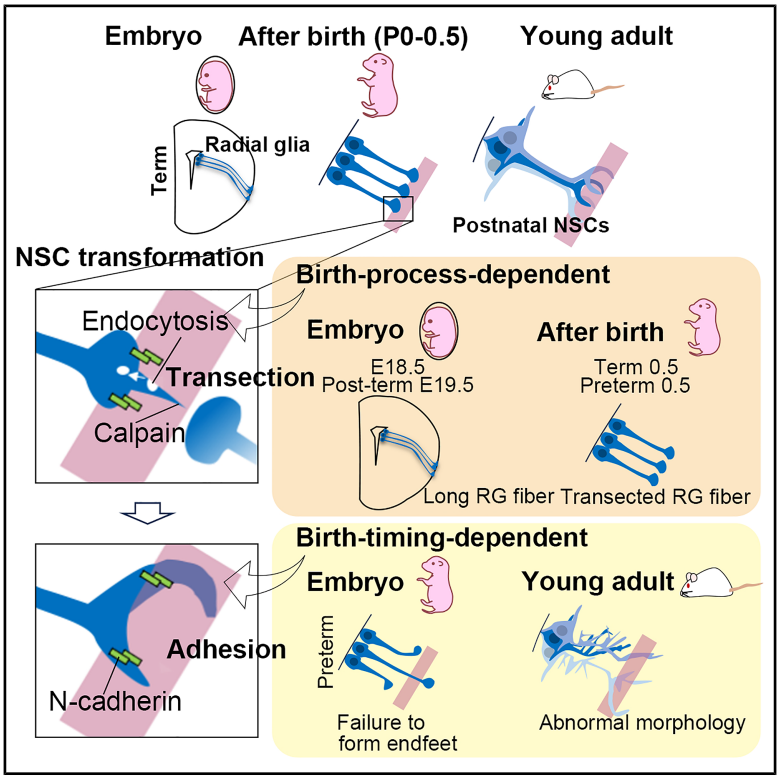
Article

Cell Reports

Transformation of radial glia into postnatal neural stem cells depends on birth

Graphical abstract



Highlights

- Radial glia (RG) transform into postnatal neural stem cells (NSCs) on the day of birth
- Calpain activity and endocytosis are crucial for birth-process-dependent RG fiber transection
- N-cadherin mediates birth-timing-dependent RG endfoot formation on blood vessels
- 3D ultrastructural analysis of the ventricular-subventricular zone reveals NSC niche details

Authors

Shoko Takemura, Koya Kawase, Laura Wolbeck, ..., Nobuhiko Ohno, Konstantin Khodosevich, Kazunobu Sawamoto

Correspondence

sawamoto@med.nagoya-cu.ac.jp

In brief

Takemura et al. demonstrate that the birth process triggers the transformation of radial glia (RG)-to-postnatal neural stem cells (NSCs) through calpain- and endocytosis-mediated fiber transection. Importantly, RG adhesion to endothelial cells via N-cadherin depends on birth timing; preterm birth disrupts this, impairing NSC morphology and reducing stemness in adulthood.

Takemura et al., 2025, Cell Reports ■■, 116029
■■, 2025 © 2025 The Author(s). Published by Elsevier Inc.
https://doi.org/10.1016/j.celrep.2025.116029

CellPress

Please cite this article in press as: Takemura et al., Transformation of radial glia into postnatal neural stem cells depends on birth, Cell Reports (2025), https://doi.org/10.1016/j.celrep.2025.116029

Cell Reports

CellPress
OPEN ACCESS

Article

Transformation of radial glia into postnatal neural stem cells depends on birth

Shoko Takemura,[1,2,3,4,16] Koya Kawase,[1,5,16] Laura Wolbeck,[6,16] Yasuhisa Nakamura,[1,5,7,16] Mami Matsumoto,[1,2] Hideo Jinnou,[1,5,8] Aika Tahara,[1] Masato Sawada,[1,2] Yoshiaki Kubota,[9] Vicente Herranz-Pérez,[10,11] José Manuel García-Verdugo,[10,17] Nobuyuki Ishibashi,[8,12] Vittorio Gallo,[8,13] Nobuhiko Ohno,[14,15] Konstantin Khodosevich,[6] and Kazunobu Sawamoto[1,2,18,*]

[1]Department of Developmental and Regenerative Neurobiology, Institute of Brain Science, Nagoya City University Graduate School of Medical Sciences, 1 Kawasumi, Mizuho-cho, Mizuho-ku, Nagoya, Aichi 467-8601, Japan
[2]Division of Neural Development and Regeneration, National Institute for Physiological Sciences, Myodaiji, Okazaki, Aichi 444-8585, Japan
[3]Department of Developmental Biology, Fujita Health University School of Medicine, Toyoake, Aichi 470-1192, Japan
[4]Division of Developmental Neurobiology, International Center for Brain Science (ICBS), Fujita Health University, Toyoake, Aichi 470-1192, Japan
[5]Department of Pediatrics and Neonatology, Nagoya City University Graduate School of Medical Sciences, 1 Kawasumi, Mizuho-cho, Mizuho-ku, Nagoya, Aichi 467-8601, Japan
[6]Biotech Research & Innovation Centre (BRIC), Faculty of Health and Medical Sciences, University of Copenhagen, 2200 Copenhagen, Denmark
[7]Department of Pediatrics, Nagoya City University West Medical Center, 1-1-1 Hiratecho, Kita-ku, Nagoya, Aichi 462-8508, Japan
[8]Center for Neuroscience Research, Children's National Research Institute, Children's National Hospital, Washington, DC 20010, USA
[9]Department of Anatomy, Keio University School of Medicine, Tokyo 160-8582, Japan
[10]Laboratory of Comparative Neurobiology, Institute Cavanilles of Biodiversity and Evolutionary Biology, CIBERNED-ISCIII, University of Valencia, 46980 Paterna, Spain
[11]Department of Cell Biology, Functional Biology and Physical Anthropology, CIBERNED-ISCIII, University of Valencia, 46100 Burjassot, Spain
[12]Department of Anatomy and Neurobiology, Boston University Chobanian and Avedisian School of Medicine, Boston, MA 02118, USA
[13]Seattle Children's Research Institute, Seattle Children's Hospital, Seattle, WA 98101, USA
[14]Division of Ultrastructural Research, National Institute for Physiological Sciences, Myodaiji, Okazaki, Aichi 444-8787, Japan
[15]Department of Anatomy, Division of Histology and Cell Biology, School of Medicine, Jichi Medical University, Shimotsuke, Tochigi 329-0498, Japan
[16]These authors contributed equally
[17]Deceased July 7, 2025
[18]Lead contact
*Correspondence: sawamoto@med.nagoya-cu.ac.jp
https://doi.org/10.1016/j.celrep.2025.116029

SUMMARY

A common feature of various postnatal stem cells is their close association with blood vessels. Postnatal neural stem cells (NSCs) in the ventricular-subventricular zone originate from fetal radial glia (RG), which possess NSC properties. Here, using live imaging and three-dimensional (3D) electron microscopy, we investigated how RG convert into postnatal NSCs and characterized the fine 3D morphology of the ventricular-subventricular zone. We found that preterm birth disrupts RG-endothelial cell interactions during this transformation, impairing both the structure and stemness of adult NSCs. These findings underscore the importance of a birth-dependent transformation. Our results indicate that RG fiber transection, which depends on the birth process, and endfoot formation on blood vessels, which depends on birth timing, are both critical steps in the conversion of RG into adult NSCs.

INTRODUCTION

Proximity to vascular structures is a common feature of many adult stem cell niches. Similar to mesenchymal and hematopoietic stem cells,[1] the maintenance of postnatal neural stem cells (NSCs) in two principal brain regions—the ventricular-subventricular zone (V-SVZ) adjacent to the lateral ventricles and the subgranular zone of the hippocampal dentate gyrus—also relies on their interactions with the vasculature.[2–5] Within the V-SVZ, postnatal NSCs exhibit a bipolar and complex morphology: on the basal side, they extend a fiber with an endfoot adhering to vascular endothelial cells,[6,7] whereas on the apical side, they project a short fiber that reaches the cerebrospinal fluid and is surrounded by a rosette of ependymal cells with broad apical surfaces, forming a pinwheel structure.[6] However, the morphogenetic mechanisms through which adult stem cells associate with blood vessels remain poorly understood.

Postnatal NSCs are generated through the transformation of fetal radial glia (RG).[8] Fetal RG cell bodies are located near the ventricular surface and extend long fibers through the

This is an open access article under the CC BY-NC-ND license (http://creativecommons.org/licenses/by-nc-nd/4.0/).

Please cite this article in press as: Takemura et al., Transformation of radial glia into postnatal neural stem cells depends on birth, Cell Reports (2025), https://doi.org/10.1016/j.celrep.2025.116029

parenchyma toward the pial surface of the brain.[9] In contrast, postnatal NSCs possess shorter fibers that terminate on blood vessels at the basal surface of the V-SVZ. This transformation involves dramatic morphological changes; however, it remains unclear precisely when and how RG shorten their long fibers and establish interactions with blood vessels. Given that mammals experience profound environmental changes at birth, we hypothesized that birth itself triggers the transformation of RG into postnatal NSCs.

RESULTS

RG fibers are transected and form endfeet on blood vessels on the day of birth

RG cells transform into postnatal NSCs during the perinatal period, but the precise timing and underlying mechanism remain unclear. To characterize this transformation, we performed *in utero* electroporation of enhanced green fluorescent protein (EGFP)-expressing plasmids into ventricular wall cells of E17.5 mouse embryos (Figures 1A and 1B). RG fiber length remained comparable between E18.5 and immediately after birth (P0, 0 h) but was significantly shorter 6 h after birth (P0.25) (Figures 1C and 1D), indicating rapid fiber shortening in the V-SVZ after birth.

To determine whether this fiber shortening depends on the timing of birth or the birth process itself, we induced preterm birth using mifepristone. RG fibers were significantly shorter in both preterm-born P0.5 (preterm P0.5) mice and term-born P0.5 (term P0.5) mice compared to those in E18.5 mice (Figures 1E–1G). These results suggest that birth triggers RG fiber shortening, even in mice delivered before the expected date. Furthermore, RG fibers in cesarean section-delivered preterm P0.5 mice were also significantly shorter than those in E18.5 mice (Figures S1A–S1C), indicating that RG fiber shortening results from the birth process itself rather than from mifepristone exposure. Consistent with these morphological changes, gene set enrichment analysis (GSEA) of our previously published single-cell RNA sequencing (scRNA-seq) data[10] revealed significant upregulation of Gene Ontology (GO) terms related to morphogenesis in RG from preterm P0.5 relative to E18.5 (Figures S1D–S1H; Table S1, sheet 1). In contrast, prolonging gestation with progesterone prevented RG fiber shortening at the expected time of birth (Figures 1H–1J), further supporting the notion that fiber shortening depends on the birth process rather than birth timing. Next, we investigated the environmental factors contributing to RG fiber transection. In agreement with the hypoxic nature of the intrauterine environment relative to the extrauterine environment,[11] we previously reported a significant elevation in partial pressure of oxygen (pO_2) within the V-SVZ after birth.[10] Therefore, we hypothesized that this postnatal oxygen increase contributes to RG fiber shortening. Indeed, blocking the postnatal oxygen elevation in cultured V-SVZ slices inhibited RG fiber transection (Figures 1K and 1L), supporting the conclusion that oxygen elevation is a critical factor in this process.

Next, we examined the cellular mechanisms responsible for RG fiber shortening. At low magnification, RG fibers at E18.5 appeared long and continuous, consistent with previous reports.[9] In contrast, at both term and preterm P0.5, shortened RG fibers and detached distal segments were visible (Figure S1I), indicating that RG fiber shortening occurred through transection rather than simple retraction. Live imaging revealed progressive RG fiber thinning, the formation of varicosity-like structures, and subsequent transection at these sites (Figures 1M and 1N; Video S1). Most fibers underwent transection within 6 h in culture (Figure 1O). In *Drosophila*, dendrite thinning is mediated by local endocytosis, and the protease calpain is responsible for the subsequent transection.[12] Consistent with this mechanism, RG fiber transection was suppressed by calpain inhibitor III, which targets calpain 1 and 2, as well as by the endocytosis inhibitor myristyl trimethyl ammonium bromide (MiTMAB) (Figures 1P–1S). Knockdown (KD) of *Cltc*, which encodes the clathrin heavy chain essential for endocytosis, significantly impaired RG fiber transection at P0.5 (Figures 1T, 1U, and S1J–S1L). Clathrin-mediated endocytosis primarily depends on post-translational modifications and conformational changes rather than transcriptional modulation.[13,14] Indeed, comparison of RG from preterm P0.5 to term E18.5 mice showed a lack of transcriptional upregulation of endocytosis-related GO terms (Table S1, sheet 1), suggesting that endocytosis is largely regulated at the post-translational level. On the day of birth, RG fiber length approximated 100 μm, roughly corresponding to the thickness of the V-SVZ (Figures 1D, 1G, 1J, 1L, 1O, 1Q, 1S, and 1U). Together, these findings indicate that birth-associated elevation in oxygen concentration promotes RG fiber transection through mechanisms dependent on calpain activity and endocytosis.

We subsequently investigated the formation of each RG endfoot on blood vessels. The proportion of RG with an endfoot on blood vessels significantly increased within 6 h after birth (P0.25) relative to immediately after birth (P0, 0 h; Figures 2A–2C), suggesting rapid endfoot formation during this early postnatal period. Most blood vessels in the V-SVZ were identified as $CD31^+Mfsd2a^+ACTA2^-$ capillaries (86.8%), with smaller fractions being $CD31^+ACTA2^+$ arteries/arterioles (9.1%) and $CD31^+Mfsd2a^-ACTA2^-$ veins/venules (4.1%). Consistent with this vascular distribution, RG endfeet predominantly formed on capillaries (Figures S2A and S2B). To further elucidate the process of endfoot formation, we performed live imaging. This analysis showed that RG fibers initially underwent transection, followed by enlargement of the endfoot at the truncated ends (Figures 2D and 2E; Video S2). Additional examination using three-dimensional (3D) reconstruction of serial block-face scanning electron microscopy (SBF-SEM) images enabled visualization of detailed RG morphology at ultrastructural resolution (Figures 2F, 2G, and S2C–S2E). SBF-SEM enables reconstruction of the complete morphology of individual cells at electron microscopic resolution. At 6 h after birth (P0.25), we observed two distinct RG-to-endothelial contact patterns: one subset of RG retained long fibers contacting only along the mid-fiber region, whereas in the other subset, each RG displayed an enlarged endfoot in direct contact with endothelial cells (Figures 2H and S2D). The contact surface area was significantly larger in RG that formed an endfoot than in those with persistent long fibers (Figure 2I). At 0 h after birth, the long-fiber subset predominated, and endfeet were rarely observed

Please cite this article in press as: Takemura et al., Transformation of radial glia into postnatal neural stem cells depends on birth, Cell Reports (2025), https://doi.org/10.1016/j.celrep.2025.116029

CellPress
OPEN ACCESS

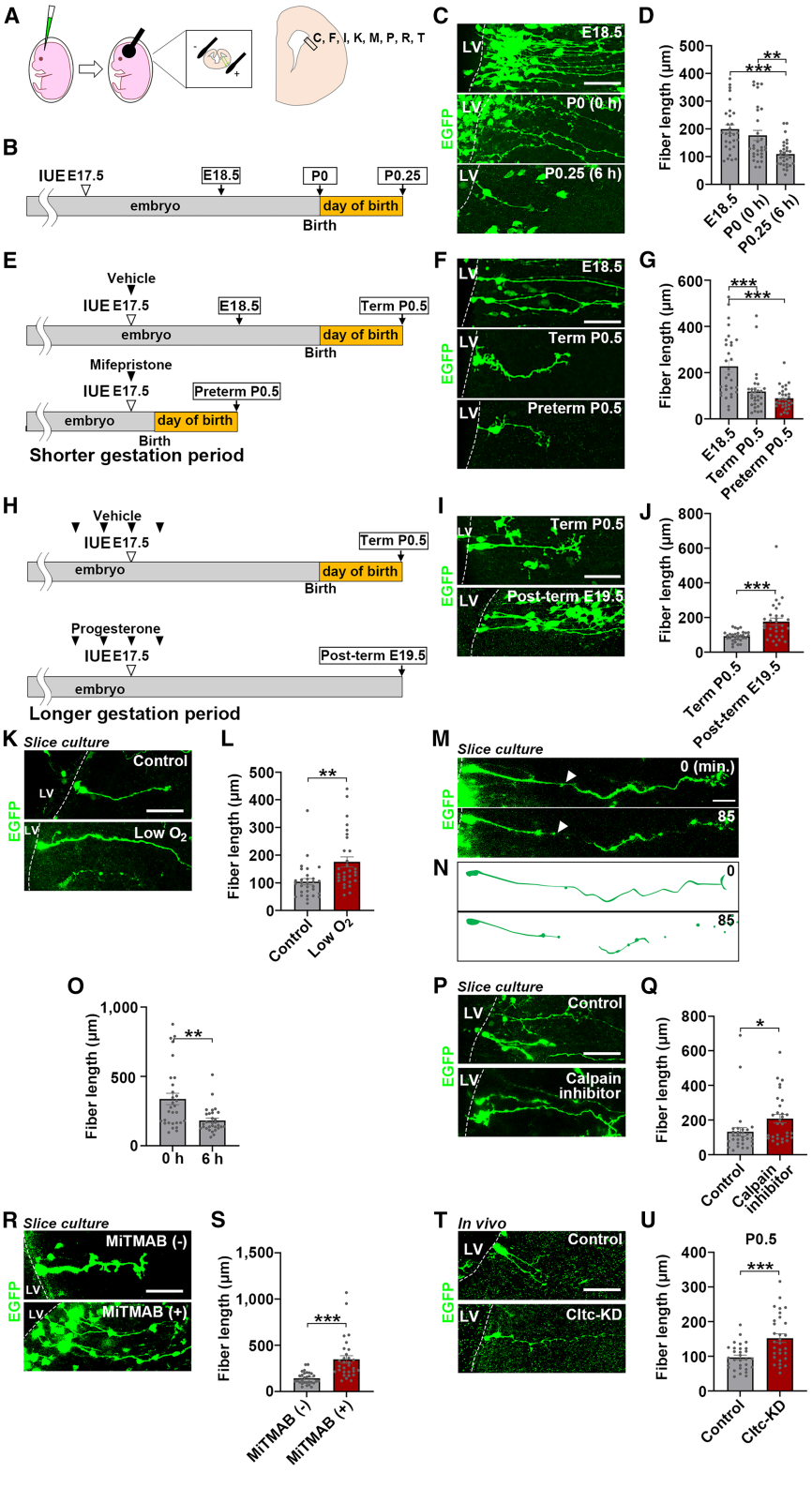


Figure 1. RG fibers are transected in an endocytosis-dependent manner on the day of birth

(A) *Left*: Schematic illustrating the *in utero* electroporation method. *Right*: Coronal section of the V-SVZ indicating regions analyzed in (C), (F), (I), (K), (M), (P), (R), and (T).

(B) Experimental timeline.

(C) Representative images of EGFP$^+$ RG in the V-SVZ at E18.5, P0 (0 h after birth), and P0.25 (6 h after birth).

(D) Quantification of fiber length in EGFP$^+$ RG in the V-SVZ.

(E) Experimental timeline. Mifepristone was administered at E17.5 to induce preterm birth.

(F) Representative images of EGFP$^+$ RG in the V-SVZ at E18.5, term P0.5, and preterm P0.5.

(G) Quantification of RG fiber length in the V-SVZ at E18.5, term P0.5, and preterm P0.5.

(H) Experimental timeline. Progesterone was administered from E15.5 to E18.5 to delay birth.

(I) Representative images of EGFP$^+$ RG in the V-SVZ at term P0.5 and post-term E19.5.

(J) Quantification of RG fiber length in the V-SVZ at term P0.5 and post-term E19.5.

(K) Representative images of RG in the V-SVZ cultured with or without an oxygen absorber.

(L) Effect of oxygen absorption on RG fiber length in the V-SVZ after 6 h of culture.

(M) Time-lapse images of EGFP$^+$ RG in a coronal brain slice. Arrowheads indicate sites of RG fiber transection.

(N) Illustration corresponding to (M).

(O) Quantification of RG fiber length in the V-SVZ at 0 and 6 h after the beginning of culture.

(P) Representative images of RG in the V-SVZ cultured with or without calpain inhibitor III.

(Q) Effect of calpain inhibitor III on RG fiber length in the V-SVZ after 6 h of culture.

(R) Representative images of RG in the V-SVZ cultured with or without MiTMAB.

(S) Effect of the endocytosis inhibitor MiTMAB on RG fiber length in the V-SVZ after 6 h of culture.

(T) Representative images of control and *Cltc*-KD RG in the V-SVZ at P0.5.

(U) Effect of *Cltc*-KD on RG fiber length in the V-SVZ at P0.5. IUE, *in utero* electroporation; LV, lateral ventricle. Scale bars, 50 μm (C, F, I, K, M, P, R, T). $^{**}p < 0.01$, $^{***}p < 0.001$. Error bars, mean ± SEM. See also Figure S1.

(Figure S2C). These data suggest that RG fiber transection precedes endfoot formation and is essential for establishing robust interactions between RG and endothelium.

We next sought to identify molecular mediators involved in endfoot formation by analyzing the expression of cell adhesion-related genes (GO term: "cell adhesion") using our previously published term P2 V-SVZ scRNA-seq dataset.[10] Several adhesion-related genes, including *Itga6* (encoding α6 integrin), *Itgb1* (encoding β1 integrin), and *Vcam1*, were expressed in RG, while endothelial cells/pericytes expressed *Cldn5* (encoding claudin-5) and *Cdh5* (encoding vascular endothelial-cadherin; Table S1, sheet 2), consistent

Please cite this article in press as: Takemura et al., Transformation of radial glia into postnatal neural stem cells depends on birth, Cell Reports (2025), https://doi.org/10.1016/j.celrep.2025.116029

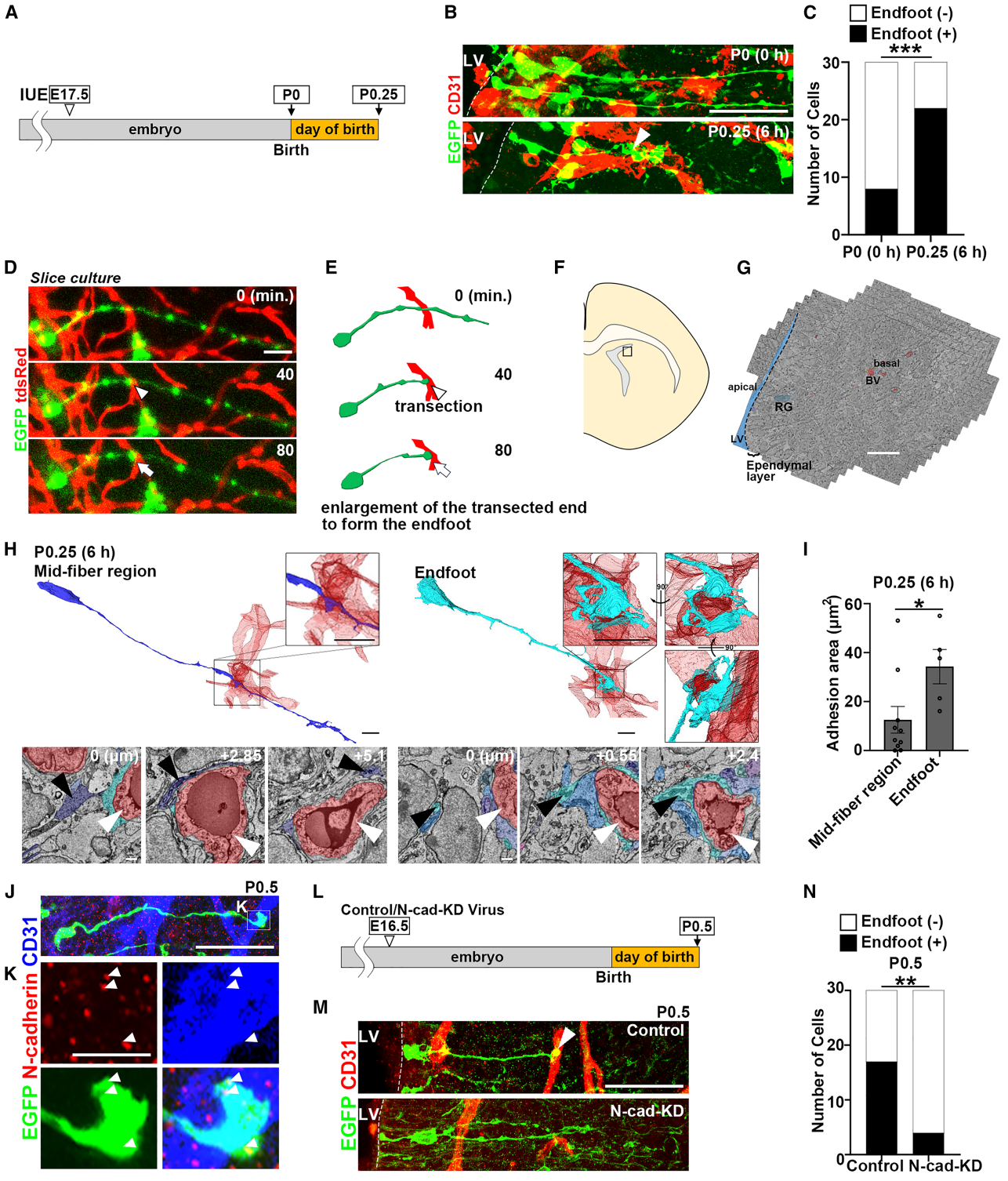


Figure 2. RG fibers form endfeet in an N-cadherin-dependent manner

(A) Experimental schematic.

(B) Representative images of RG endfoot (arrowhead) and CD31-expressing endothelial cells in the V-SVZ at P0 (0 h after birth) and P0.25 (6 h after birth).

(C) Quantification of RG each forming an endfoot in the V-SVZ at P0 (0 h after birth) and P0.25 (6 h after birth).

(legend continued on next page)

Please cite this article in press as: Takemura et al., Transformation of radial glia into postnatal neural stem cells depends on birth, Cell Reports (2025), https://doi.org/10.1016/j.celrep.2025.116029

with previous studies.[3,15–17] Differentially expressed gene (DEG) analysis further revealed dynamic transcriptomic changes around the time of birth (Table S1, sheet 3,4; E18.5 and term P2.5 samples). Notably, *Cdh2*, which encodes N-cadherin—an adhesion molecule expressed in both NSCs[18] and endothelial cells[19,20]—was among the most highly expressed adhesion-related genes in both RG and endothelial cell/pericyte clusters at term P2. Immunohistochemical analysis confirmed N-cadherin expression in both RG endfeet and endothelial cells at P0.5 (Figures 2J and 2K). KD of *Cdh2* in RG significantly reduced the proportion of RG forming endothelial endfeet relative to controls at P0.5 (Figures 2L–2N and S2F), without affecting fiber transection or contact with the ventricular surface (Figures S2G–S2I). Furthermore, conditional knockout of *Cdh2* in endothelial cells using *Cdh5-Cre^{ERT2};Cdh2^{floxed}* mice similarly impaired RG endfoot formation (Figures S2J–S2L). These results demonstrate that N-cadherin expression in both RG and endothelial cells is essential for robust RG-endothelial adhesion; endothelial cells serve as anchoring structures for RG fibers through N-cadherin-mediated interactions. Our findings indicate that each radial glial cell forms an endfoot on blood vessels on the day of birth, a process critically dependent on N-cadherin-mediated adhesion. In summary, the transformation of RG into postnatal NSCs in the V-SVZ is initiated on the day of birth.

Normal morphology of postnatal NSCs depends on birth timing

To investigate the detailed morphology and cellular interactions of postnatal NSCs in the V-SVZ of young adult mice, we reconstructed the 3D SBF-SEM images (Figures 3A, 3B, and S3A). Individual cell types were identified according to previously established criteria,[21] and comprehensive 3D structures were reconstructed for the V-SVZ of term-born mice at P28.5 (term P28.5) (Figures 3C and S3B; Video S3). We identified four distinct patterns of adhesion between NSCs and surrounding cells, organized from the apical to the basal aspects of the V-SVZ: 1) at the apical surface, NSCs were positioned at the center of the ependymal pinwheel and adhered to one another within the ependymal cell layer (Figures 3C and 3D); 2) slightly more basally, NSCs—including those from adjacent pinwheels—formed cohesive sheets encasing a chain of new neurons (Figures 3C and 3E–3G); 3) in the deeper basal region of the V-SVZ, NSC fibers were arranged into bundles, where fibers from inner NSCs were enclosed by those of outer NSCs in a layered structure (Figures 3C, 3I–3K, S3C, and S3D); and 4) at the most basal level, NSC fibers were defasciculated and individually adhered to blood vessels, forming extensive endfoot contacts with endothelial cells (Figures 3C, 3E, 3I, 3J, 3L, 3M, S3C, and S3E; Table S1, sheet 5). These observations indicate that young adult NSCs adhere to one another and undergo defasciculation on the basal side of the V-SVZ to establish endfoot contact with vascular endothelial cells.

To determine whether the morphology of adult NSCs is influenced by birth timing, we compared SBF-SEM data from term P28.5 and preterm-born P29.5 (preterm P29.5) V-SVZ (Figures 3, 4A–4H, S3A, S3E, and S3F; Video S4). First, on the apical side, NSCs assembled at the center of the ependymal pinwheel and adhered to one another, similar to term P28.5 NSCs (Figures 4A and 4B). Second, the sheet of NSCs surrounding a chain of new neurons appeared partially disrupted (Figures 4A and 4C–4F). Third, on the more basal side of the V-SVZ, each NSC fiber exhibited extensive branching, and the bundled organization of NSC fibers was partially disorganized (Figures 4A, 4C, and 4G). Fourth, most NSCs in preterm P29.5 mice lacked an endfoot on blood vessels, despite their proximity to the vasculature (Figures 4C, 4G, 4H, and S3F; Table S1, sheet 5). Quantitative analysis of confocal microscopy images confirmed increased fiber branching and a higher proportion of NSCs without endfeet in preterm-born mice (Figures S3G–S3J), whereas vascular structure appeared unaltered (Figure S3K). These results suggest that proper morphogenesis of postnatal NSCs depends critically on birth timing.

NSCs differentiate into new neurons through intermediate progenitor cells,[22] and together with other astrocytes, NSCs encase chains of migrating new neurons—sometimes including intermediate progenitors—forming a structural "tunnel."[23] We further examined these tunnel structures in both term P28.5 and preterm P29.5 V-SVZ. In the term P28.5 V-SVZ, NSCs were clearly separated from new neurons (Figures 3F–3H and S3L). In contrast, NSC fibers were intermingled with new neurons in the preterm P29.5 V-SVZ (Figures 4D–4F and S3M). We next investigated whether these morphological findings are

(D) Time-lapse images of EGFP$^+$ RG and *Flt1-tdsRed*$^+$ blood vessels in a coronal brain slice. *Flt1-tdsRed* mice express dsRed in vascular endothelial cells. Transection of RG fibers (arrowheads) and subsequent enlargement of the transected end to form an endfoot (arrows) are observed.
(E) Illustration corresponding to (D).
(F) Coronal section of the V-SVZ indicating regions analyzed.
(G) Representative SBF-SEM image of the neonatal V-SVZ at P0.25 (6 h after birth).
(H) Upper: 3D rendering of RG (blue) and blood vessels (semi-transparent red) reconstructed from SBF-SEM data. The direct adhesion site between the RG and vascular endothelial cells is highlighted in red. Lower: 2D images showing RG fibers (semi-transparent blue) and blood vessels (semi-transparent red). Left panels show RG (closed arrowheads) with long fibers partially contacting endothelial cells (open arrowheads) along their length. Right panels show RG (closed arrowheads) with an enlarged endfoot contacting endothelial cells (open arrowheads).
(I) Quantification of adhesion area between RG and endothelial cells at P0.25.
(J) Localization of N-cadherin in RG and CD31-expressing endothelial cells in the V-SVZ at P0.5.
(K) Magnified view of the boxed region in (J). Arrowheads indicate N-cadherin immunoreactivity.
(L) Experimental schematic. To selectively infect RG adjacent to the lateral ventricles, N-cadherin-KD lentivirus was injected into the lateral ventricle at E16.5. Morphological analysis of RG was performed at P0.5.
(M) Representative images showing the effect of N-cadherin knockdown (KD) on an endfoot formation in each RG in the V-SVZ at P0.5.
(N) Quantification of endfoot-forming RG in control and N-cadherin-KD conditions at P0.5. IUE, *in utero* electroporation; LV, lateral ventricle. Scale bars: 1 μm (H: 2D images), 10 μm (G, H: 3D images, and K), 50 μm (B, D, J, M). *$p < 0.05$, **$p < 0.01$, ***$p < 0.001$. See also Figure S2.

Please cite this article in press as: Takemura et al., Transformation of radial glia into postnatal neural stem cells depends on birth, Cell Reports (2025), https://doi.org/10.1016/j.celrep.2025.116029

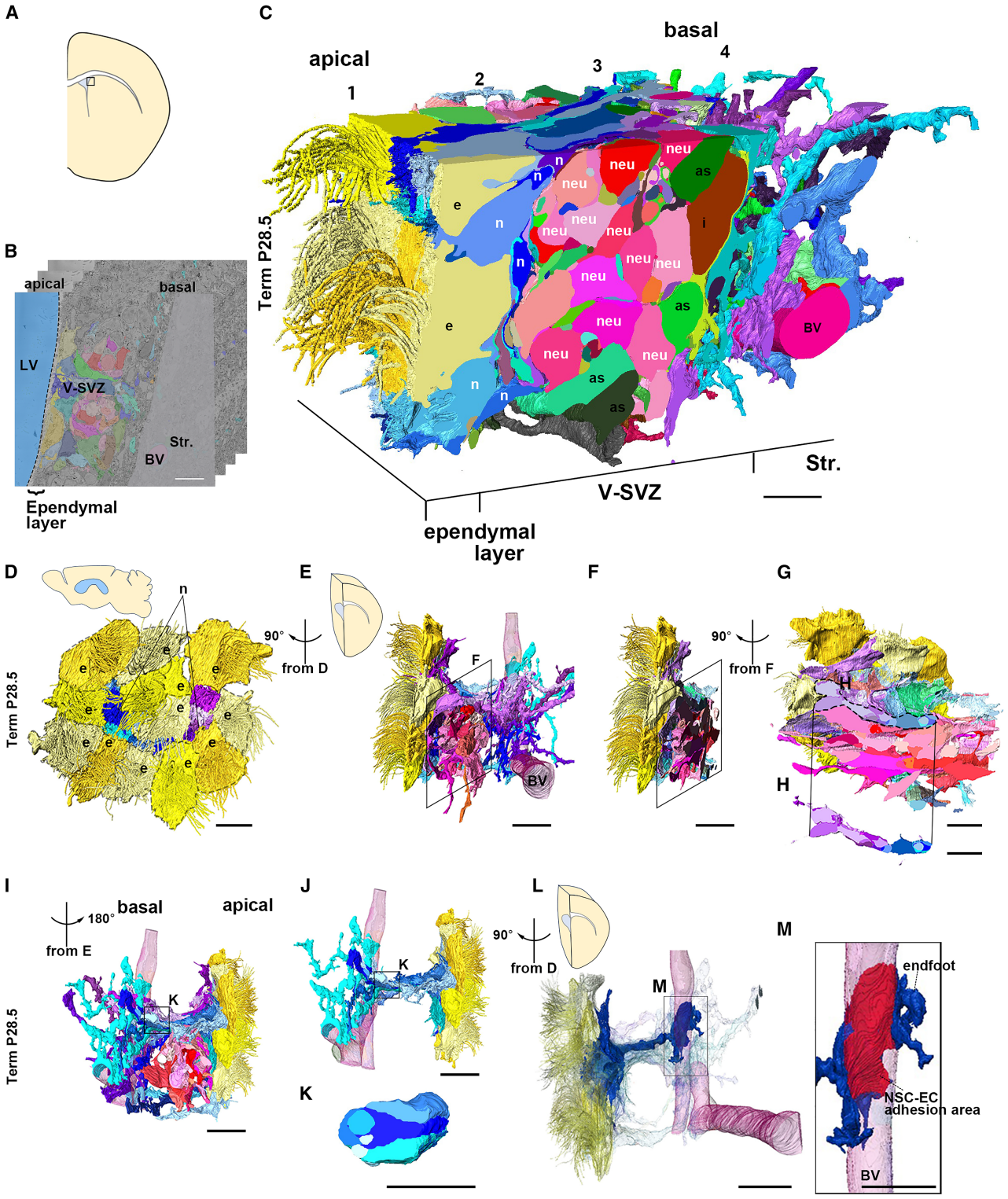


Figure 3. Normal morphology of the whole V-SVZ containing postnatal NSCs

(A) Coronal section of the V-SVZ indicating regions analyzed.

(B) Representative SBF-SEM image of the young adult V-SVZ (term P28.5).

(C) 3D rendering of the V-SVZ reconstructed from SBF-SEM data. Numbers correspond to those in the main text.

(legend continued on next page)

Please cite this article in press as: Takemura et al., Transformation of radial glia into postnatal neural stem cells depends on birth, Cell Reports (2025), https://doi.org/10.1016/j.celrep.2025.116029

conserved in humans. In human infants, the V-SVZ contains dense clusters of doublecortin (DCX)$^+$ migrating new neurons.[24] Similar to the term-born mouse V-SVZ, vimentin$^+$ glial fibers surrounded DCX$^+$ cell clusters in term-born human infants (Figures S3N–S3P). In contrast, vimentin$^+$ glial fibers were intermingled with DCX$^+$ cells in preterm-born human infants, although no significant difference was observed in DCX$^+$ cell density (Figures S3N–S3U). These results suggest that preterm birth disrupts the morphological integrity of NSCs and their tunnel-like organization for chains of migrating neurons in both mouse and human V-SVZ.

Finally, considering the morphological abnormalities observed in preterm-born mice, we performed scRNA-seq to analyze gene expression profiles in the entire V-SVZ of term P28.5 and preterm P29.5 mice. Clustering and cell type assignment were conducted based on known marker genes (Figures 4I and S4A–S4I).[25] GSEA revealed significant downregulation of cell adhesion-related GO terms in NSCs/astrocytes and endothelial cells from preterm P29.5 mice compared with term P28.5 mice (Figures 4J, 4K, and S4J–S4M; Table S1, sheet 6,7). These transcriptomic findings align with our morphological observations and support the presence of impaired cell adhesion mechanisms in the preterm-born V-SVZ (Figures 3, 4A–4H, S3A, S3E, and S3F; Video S4).

Overall, these results demonstrate that proper morphological maturation of postnatal NSCs, as well as their adhesive interactions with vascular endothelial cells and neighboring NSCs, strongly depend on birth timing.

Adhesion of RG to blood vessels on the day of birth is important for the morphogenesis and neurogenic activity of postnatal NSCs

We next investigated whether birth timing influences RG endfoot formation on blood vessels. The percentage of RG each forming an endfoot on endothelial cells was significantly lower in preterm P0.5 mice than in term P0.5 mice (Figures 5A and 5B). Immunofluorescence analysis revealed higher N-cadherin expression in RG from term P0.5 mice compared to that from E18.5, preterm P0.5, and preterm P1.5 mice (Figures 5C and 5D). Furthermore, DE analysis using our previously published scRNA-seq dataset[10] showed significantly lower expression of *Cdh2* in RG from preterm P3 mice relative to term P2 mice (Table S1, sheet 8,9), suggesting impaired N-cadherin expression in RG of preterm animals. Vascular parameters—including vessel density, length, and branching—did not significantly differ between term and preterm P0.5 mice (Figure S5A), suggesting that preterm birth induces a specific dysregulation of N-cadherin expression in RG, rather than reflecting a simple developmental delay. Based on these findings, we hypothesized that reduced N-cadherin expression in RG on the day of birth disrupts proper NSC morphogenesis and limits their neurogenic potential.

To test this hypothesis, we performed lentivirus-mediated KD of N-cadherin in RG (Figure S5B). N-cadherin KD significantly reduced RG endfoot formation on blood vessels and resulted in abnormal morphology of postnatal NSCs in term-born mice (Figures 5E–5G, S5C, and S5D). Additionally, N-cadherin KD led to decreased densities of EGFP$^+$/glial fibrillary acidic protein (GFAP)$^+$/epidermal growth factor receptor (EGFR)$^+$/Mash1$^+$ active and neurogenic NSCs, as well as EGFR$^+$/Mash1$^+$ intermediate progenitor cells, while the overall density of EGFP$^+$GFAP$^+$ NSCs was unaltered in the term P28.5 V-SVZ (Figures 5H, 5I, S5E, and S5F). These results suggest that RG adhesion to blood vessels via N-cadherin on the day of birth is critical for proper endfoot formation and neurogenic activity of NSCs in young adults, recapitulating the phenotype observed in preterm-born mice.

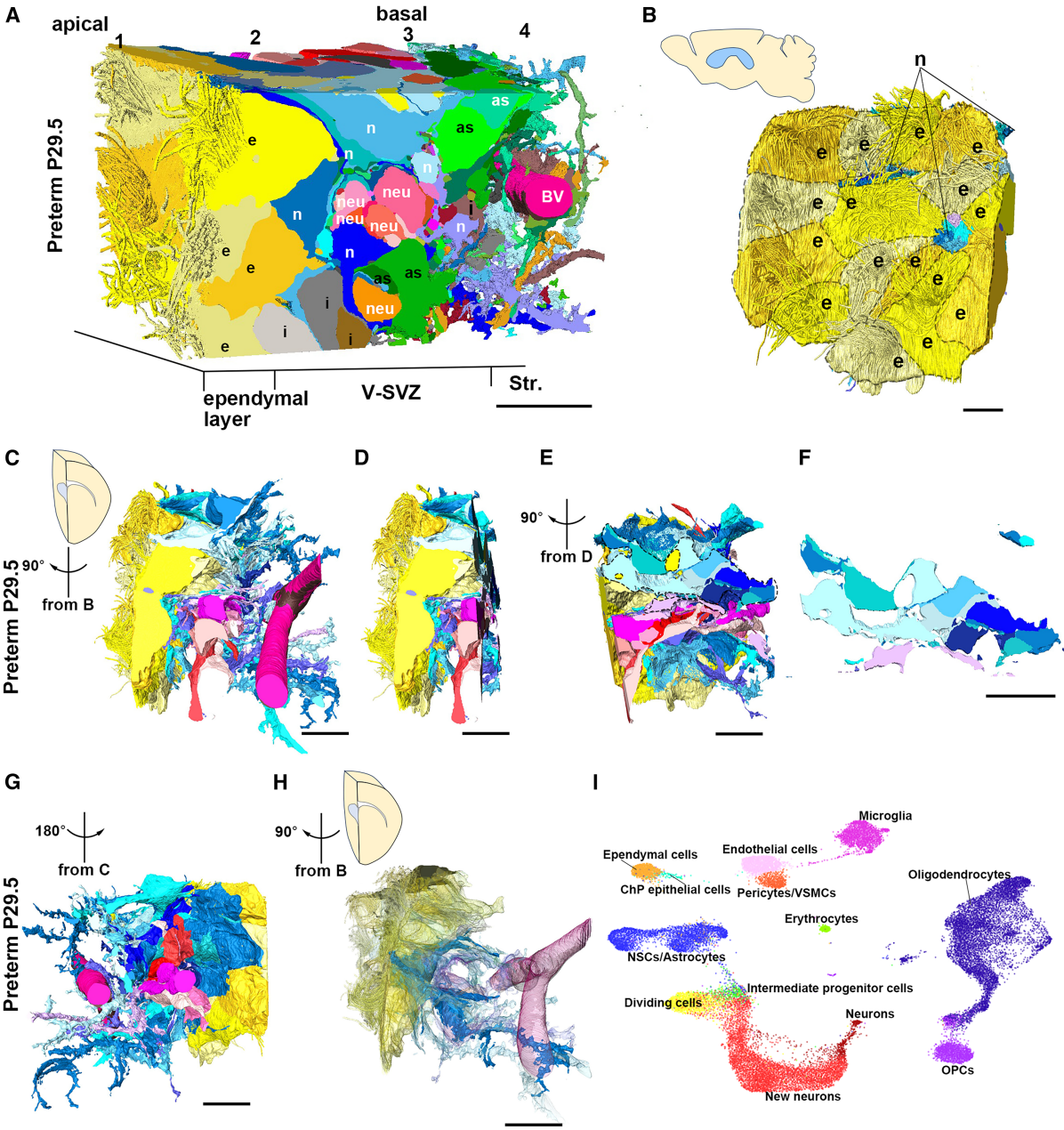
DISCUSSION

The results of this study demonstrate that birth is essential for initiating the conversion of RG into postnatal NSCs; it influences their subsequent morphogenesis and neurogenic activity. Although it is well-established that postnatal NSCs in the V-SVZ originate from embryonic RG, the precise mechanisms governing this transformation remain unclear. Here, we show that RG fibers in the V-SVZ undergo transection within 6 h after birth. In *Drosophila*, dendrites of larval sensory neurons are transected similarly within 5 h after puparium formation, enabling their transformation into adult sensory neurons during larval-to-adult metamorphosis.[26] These observations suggest that major developmental transitions—such as birth in mice and pupation in *Drosophila*—initiate tightly regulated spatiotemporal morphogenetic events required to establish mature cellular morphology.

Additionally, sensory neurons selectively eliminate unwanted larval dendrites via endocytosis and calpain activity in *Drosophila*, reutilizing the remaining cellular components.[26] Similarly, our

(D) Pinwheel structure viewed from the lateral ventricle side of the V-SVZ. NSCs (blue) and ependymal cells (yellow). Dashed lines indicate boundaries of ependymal cells.
(E) Coronal view showing NSCs (blue), ependymal cells (yellow), new neurons (red), and blood vessels, including endothelial cells (semi-transparent pink).
(F) Cross-sectional view corresponding to (E).
(G) View of (F) rotated by 90°. Dashed line indicates the position of the cross-sectional view shown in (H).
(H) View of NSCs forming a continuous sheet through mutual adhesion.
(I) View of (E) rotated by 180°.
(J) View of (I) without new neurons.
(K) Cross-sectional view of bundled NSC fibers shown in the boxed region of (I) and (J).
(L) Representative image showing one NSC (blue), other NSCs (semi-transparent blue), ependymal cells (semi-transparent yellow), and blood vessels (semi-transparent pink).
(M) Magnified view of the boxed region in (L), showing the NSC endfoot. The direct adhesion site between the NSC endfoot and vascular endothelial cells is highlighted in red. as, astrocyte; BV, blood vessel (including endothelial cells); e, ependymal cell; i, intermediate progenitor cell; n, NSC; neu, new neuron. Scale bars: 5 μm (C, K, and M), 10 μm (B, D–J, and L). See also Figure S3.

Please cite this article in press as: Takemura et al., Transformation of radial glia into postnatal neural stem cells depends on birth, Cell Reports (2025), https://doi.org/10.1016/j.celrep.2025.116029



(legend on next page)

Please cite this article in press as: Takemura et al., Transformation of radial glia into postnatal neural stem cells depends on birth, Cell Reports (2025), https://doi.org/10.1016/j.celrep.2025.116029

findings indicate that RG fibers undergo transection to remove distal segments during their transformation into postnatal NSCs. Although fiber retraction—as observed during embryonic cortical development[27]—may be possible, fiber transection appears advantageous in this context because RG fibers do not need to traverse the developing striatum,[28] which could interfere with early neural circuit formation. Analogous to sensory neuron remodeling in *Drosophila*, it is likely that RG cell bodies and their remaining proximal fibers are reused to form postnatal NSCs.

Furthermore, we found that endocytosis and calpain activity—both essential mediators of dendritic pruning in *Drosophila*[12,29]—are required for RG fiber transection. Our data strongly support the notion that transection mediated by endocytosis and calpain facilitates efficient remodeling of RG fibers, representing a conserved mechanism across biological systems. Similar events are observed, for example, in macrophages during cytoplasmic division at the final stage of cell division,[12,30] and calpain activity plays a critical role in axonal cytoskeleton disassembly during Wallerian degeneration.[31] Collectively, these findings indicate that the transformation of RG into postnatal NSCs shares conserved molecular and cellular principles with the larval-to-adult remodeling of sensory neurons in *Drosophila*. These principles involve transection mediated by endocytosis and calpain, followed by reutilization of cellular components in later life stages.

The NSC niche has attracted considerable research attention. Previous studies using transmission electron microscopy identified multiple cell types in the V-SVZ[21]; confocal microscopy combined with fluorescent labeling provided broader views of these populations.[6] In this study, we used SBF-SEM to investigate the detailed 3D ultrastructure and adhesive interactions of cells in the V-SVZ. SBF-SEM and scRNA-seq analyses in young adult mice highlighted the importance of NSC-endothelial and NSC-NSC adhesion. SBF-SEM data revealed that each NSC forms an endfoot directly on blood vessels, a critical interaction for the maintenance of adult NSCs.[2,3,32] Furthermore, the 3D endfoot morphology of postnatal NSCs closely resembles that of astrocytes,[33] displaying continuous sheet-like structures that likely support adhesive interactions with the vasculature.

In the adult pinwheel structure, ependymal cells with large apical surfaces surround central clusters of multiple NSCs.[6] Considering our observation that RG fibers form bundles at P0, these bundles may give rise to the central clusters of the adult pinwheel and contribute to the maintenance of NSC-NSC adhesion after birth. On the apical side of the adult V-SVZ, this pinwheel organization—with ependymal cells radially encircling NSCs—may enable NSCs to maintain close apical contact with one another while simultaneously forming an extensive basal endfoot to interact with blood vessels. In preterm-born young adult mice, NSCs exhibited impaired adhesion to endothelial cells and neighboring NSCs, potentially contributing to stem cell dysfunction. Such compromised adhesion may be detrimental because adult NSCs are known to regulate the quiescence of neighboring NSCs.[34] In this study, we identified NSCs based on morphological criteria, although we speculate that only a subset of these morphologically defined cells retains the capacity to differentiate into intermediate progenitor cells. The detailed 3D morphology of NSCs revealed in this study enhances our understanding of the niche requirements necessary for the long-term maintenance of postnatal NSCs.

Our recent study demonstrated that preterm birth significantly reduces NSC stemness in young adults by hyperactivating neonatal NSCs, resulting in their premature depletion.[10] Given that blood- or endothelial-derived factors might regulate adult NSC quiescence,[7] and that direct endfoot contact with endothelial cells is important for maintaining this quiescent state,[3,32] the impaired endfoot formation observed in preterm neonates likely interferes with the transition of RG into quiescence. This impairment appears to result from reduced N-cadherin expression at birth, which weakens N-cadherin-dependent endfoot formation. Vascular endothelial cadherin mediates endothelial-to-endothelial adhesion, but endothelial cells also express N-cadherin, which facilitates adhesion to pericytes.[19,20] Additionally, adhesion between NSCs and ependymal cells within pinwheel structures is N-cadherin-dependent and essential for maintaining NSC quiescence.[18] While our KD of Cdh2 in RG did not significantly reduce apical contact, we found that both Cdh2 KD in RG and Cdh2 deletion in endothelial cells impaired RG endfoot formation. These findings, together with previous studies, suggest that N-cadherin contributes to adhesion at both apical and basal surfaces.

The broad expression of N-cadherin would permit efficient adhesion between RG and the vascular network at sites where RG encounter endothelial cells. Rather than specifying the

Figure 4. Adhesion of postnatal NSCs to vascular endothelial cells and surrounding NSCs is impaired by preterm birth

(A) 3D rendering of the preterm P29.5 V-SVZ reconstructed from SBF-SEM data. Numbers correspond to those in the main text.

(B) Pinwheel structure viewed from the lateral ventricle side of the V-SVZ.

(C) Coronal view showing NSCs (blue), ependymal cells (yellow), new neurons (red), and blood vessels, including endothelial cells (pink) and pericytes (brown).

(D) Cross-sectional view corresponding to (C).

(E) View of (D) rotated by 90°. The dashed line indicates the position of the cross-sectional view shown in (F).

(F) Magnified view of NSCs.

(G) View of (C) rotated by 180°.

(H) Representative image showing one NSC (blue), other NSCs (semi-transparent blue), ependymal cells (semi-transparent yellow), and blood vessels (semi-transparent pink).

(I) UMAP representation of scRNA-seq data from V-SVZ cells of term P28.5 and preterm P29.5 mice. A total of 29,127 cells were collected (14,946 from term and 14,181 from preterm samples).

(J and K) Dot plots showing enriched pathways identified by GSEA in NSCs/astrocytes (J) and endothelial cells (K). Gene ratio indicates the proportion of significant genes associated with each GO term; dot size represents the number of genes; color denotes adjusted *p* values (Benjamini–Hochberg correction). as, astrocyte; BV, blood vessel (including endothelial cells); ChP, choroid plexus; e, ependymal cell; i, intermediate progenitor cell; n, NSC; neu, new neuron; OPC, oligodendrocyte precursor cell; VSMCs, vascular smooth muscle cells. Scale bars: 10 μm. See also Figures S3 and S4.

Please cite this article in press as: Takemura et al., Transformation of radial glia into postnatal neural stem cells depends on birth, Cell Reports (2025), https://doi.org/10.1016/j.celrep.2025.116029

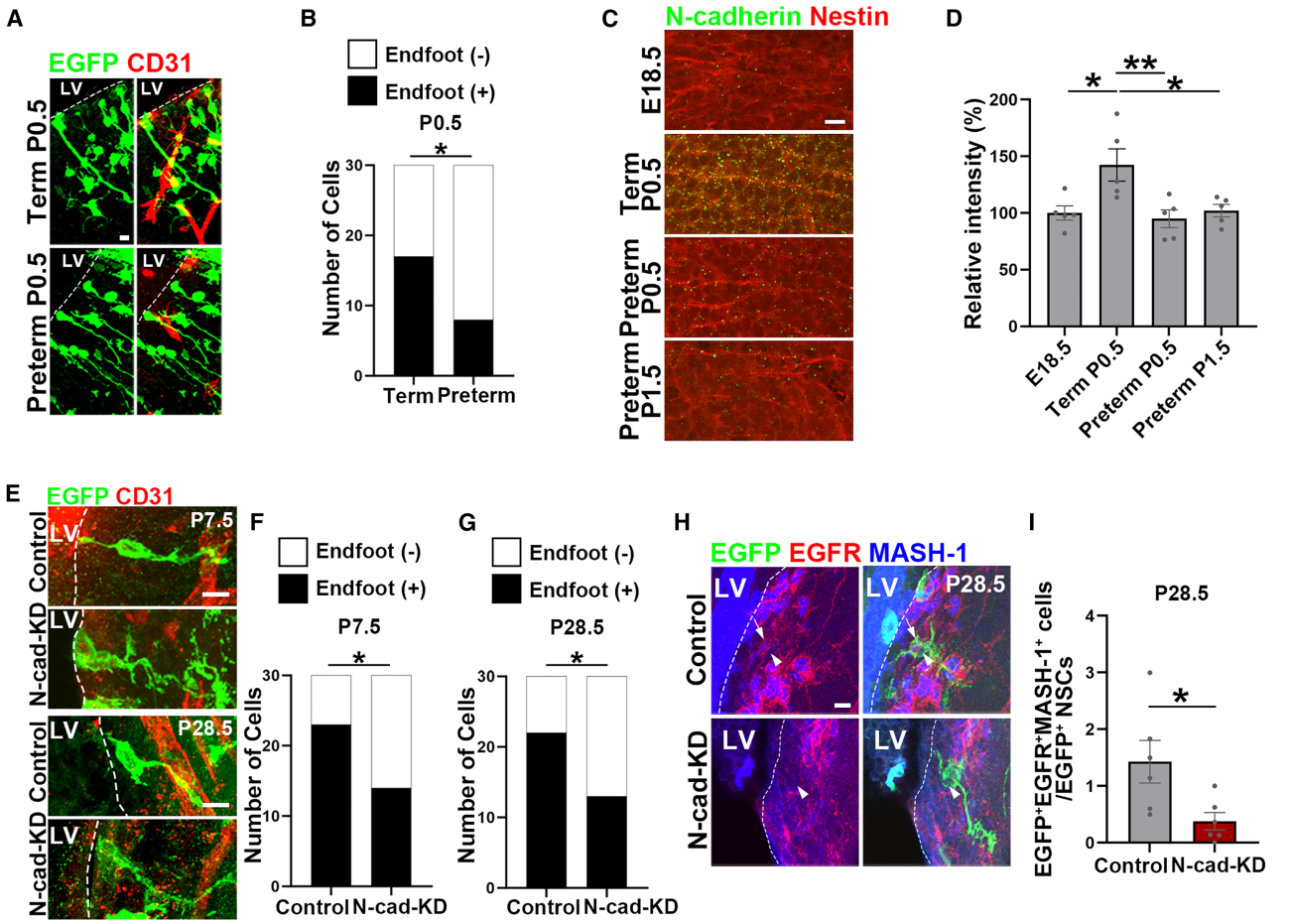


Figure 5. Low expression of N-cadherin impairs NSC morphology and stemness in preterm mice

(A) Representative images of RG in the V-SVZ at term P0.5 and preterm P0.5.

(B) Quantification of RG each forming an endfoot in the V-SVZ at term P0.5 and preterm P0.5.

(C) Representative images showing N-cadherin and nestin^{+} RG in the V-SVZ at E18.5, term P0.5, preterm P0.5, and preterm P1.5.

(D) Relative intensity of N-cadherin immunoreactivity in nestin^{+} RG at E18.5, term P0.5, preterm P0.5, and preterm P1.5.

(E) Representative images showing the effect of N-cadherin KD on NSC morphology in the V-SVZ at term P7.5 and P28.5.

(F and G) Quantification of the proportion of NSCs, each forming an endfoot in the V-SVZ at P7.5 (F) and P28.5 (G) after N-cadherin KD.

(H) Representative images of coronal V-SVZ sections stained for EGFP (green), EGFR (red), and Mash1 (blue) at P28.5. Arrows indicate EGFP^{+}/EGFR^{+}/Mash1^{+} cells whereas arrowheads indicate EGFP^{+}/EGFR^{-}/Mash1^{-} cells.

(I) Densities of EGFP^{+}EGFR^{+}Mash1^{+} cells in the V-SVZ at P28.5. LV, lateral ventricle. Scale bars: 10 μm. Error bars, mean ± SEM. See also Figure S5.

precise location of endfoot formation, N-cadherin may enable adhesion wherever physical contact occurs. A potential advantage of N-cadherin is its widespread expression across multiple regions of the cell membrane and even across distinct cell types. As a comparable example, dystroglycan has been shown to mediate interactions between fetal RG and the pial basement membrane[35] between astrocytes and endothelial cells at the blood-brain barrier[36] and between ependymal cells and NSCs at the apical surface of the V-SVZ,[37] suggesting that broadly expressed adhesion molecules such as N-cadherin are not exclusive determinants, but rather key facilitators of intercellular interactions.

In this study, we observed RG fiber transection even in cesarean section births, which are less influenced by maternal hormones and vaginal mechanical forces compared with vaginal deliveries. This finding underscores the importance of the transition from the intrauterine to the extrauterine environment in initiating NSC transformation. Among the various changes accompanying birth, changes in oxygen concentration play a critical role in regulating stem cell proliferation and differentiation.[38] Moreover, increased levels of reactive oxygen species, generated by exposure to the oxygen-rich postnatal environment, can induce cell-cycle arrest in cardiomyocytes,[39] suggesting that a similar oxidative mechanism might influence NSCs. Intriguingly, zebrafish, which inhabit a relatively hypoxic aquatic environment, retain RG with elongated fibers and maintain robust neurogenic capacity into adulthood.[40] It is thus likely that elevated oxygen levels associated with birth promote RG fiber transection and endfoot formation, directing NSCs toward a quiescent state. The transformation process—characterized by

Please cite this article in press as: Takemura et al., Transformation of radial glia into postnatal neural stem cells depends on birth, Cell Reports (2025), https://doi.org/10.1016/j.celrep.2025.116029

RG fiber transection and endfoot formation—may be essential for establishing NSC quiescence. In support of this hypothesis, our observations showed that inhibition of postnatal oxygen elevation prevented RG fiber transection. Collectively, these findings suggest that the transition from a hypoxic intrauterine environment to an oxygen-rich extrauterine environment serves as a critical factor in NSC conversion.

In addition to oxygen level, other physiological changes may contribute to RG fiber transection. For example, maternal oxytocin, a hormone implicated in shaping neuronal development in the infant brain,[41,42] can induce intracellular calcium influx.[43] Mechanical forces during vaginal delivery may also affect brain development; although direct evidence remains limited, magnetic resonance imaging studies have documented structural brain changes in infants during delivery.[44] Mechanical stress is known to activate the calcium-dependent protease calpain, which can induce axonal beading.[45] These findings raise the possibility that calcium signaling, triggered by oxytocin or mechanical stress, may activate calpain-mediated transection of RG fibers. Furthermore, as gene expression in brain tissue undergoes marked changes around birth,[46] it is also possible that transcriptional responses to birth-associated cues contribute to the RG fiber transection. Further investigation into these birth-associated molecular and mechanical transitions will be essential for understanding the mechanisms of the transformation from RG to postnatal NSCs.

The transformation of RG into "truncated RG"—defined by shortened fibers and endfoot formation on endothelial cells—has been reported in the human cerebral cortex as early as 17 weeks of gestation.[47] In ferrets, truncated RG, which display a high degree of similarity to human truncated RG based on transcriptomic analysis, appear shortly before birth and increase during the neonatal period.[48] Similarly, we observed a subset of RG in mice with shortened fibers at E18.5 and immediately after birth (0 h), suggesting that the transformation from RG to postnatal NSCs may begin prenatally. Although truncated RG in the human and ferret cerebral cortices and postnatal NSCs in the mouse V-SVZ share common features—such as shortened fibers and vascular interaction via their endfeet—the timing of their appearance differs, likely reflecting regional differences within the brain or interspecies variation. Additionally, structural abnormalities observed in the V-SVZ of preterm infants suggest that the transition from the intrauterine to the extrauterine environment also influences NSC development in humans. Notably, experimental manipulation of birth timing confirmed that RG fiber transection mainly occurs postnatally, regardless of the time elapsed since fertilization. Given that gestation lengths vary among mammalian species and can vary slightly even within the same species,[49,50] a birth-process-dependent mechanism likely represents a robust strategy to ensure precise neurodevelopment in mammals.

The present findings emphasize that "time from birth" and "time from fertilization" both substantially influence development. In mammals, stem cell populations are maintained within restricted regions after birth. Considering that many cell types undergo substantial gene expression changes on the day of birth,[51] further investigation into birth-associated transitions will deepen our understanding of the mechanisms essential for sustaining stem cell populations within their niche.

Limitations of the study

In this study, we focused on the mechanisms of adhesion between RG and endothelial cells on the day of birth, given the critical role of endothelial adhesion in the maintenance of adult NSCs.[3] We propose that N-cadherin enables RG to adhere to neighboring endothelial cells to form an endfoot. However, additional molecules and/or mechanisms are likely required to specify endfoot localization. GO analysis using scRNA-seq data revealed regional differences in the expression of genes related to cell adhesion in endothelial cells.[52] As blood-derived molecules such as prolactin and erythropoietin are known to regulate NSC stemness,[53,54] molecular and metabolic signals from endothelial cells or circulating blood may further refine the positional specificity of RG adhesion; however, these possibilities were not directly addressed in this study. Although our analysis did not reveal severe structural abnormalities in the vasculature of preterm-born animals, subtle functional or signaling alterations may have been present. Because our findings underscore the importance of RG adhesion to endothelial cells for maintaining postnatal NSCs, future studies should aim to identify additional adhesion molecules involved in the spatial specificity of RG-endothelial interactions and to investigate the broader roles of blood vessels in NSC maintenance. A more comprehensive investigation of these mechanisms will be essential for elucidating the factors that regulate postnatal NSC maintenance.

RESOURCE AVAILABILITY

Lead contact

Further information and requests for resources and reagents should be directed to and will be fulfilled by the lead contact, Kazunobu Sawamoto (sawamoto@med.nagoya-cu.ac.jp).

Materials availability

Materials generated in this study are available from the lead contact upon request, subject to a completed materials transfer agreement.

Data and code availability

- Code for the scRNA-seq analysis is available on GitHub (https://github.com/khodosevichlab/Preterm_project_2_code_repo/tree/main). Raw scRNA-seq data are available in the Sequence Read Archive (SRA) (https://www.ncbi.nlm.nih.gov/sra/PRJNA1073531).
- Interactive 3D models of the V-SVZ are shown, and printable models are available on Sketchfab:

https://sketchfab.com/3d-models/v-svz-p0-6-h-1-82e2a9feb4d049d5a2f88b65ef482e98
(P0 6 h-1).
https://sketchfab.com/3d-models/v-svz-p0-6-h-2-be91302adb31442e85f67436e90623ba
(P0 6 h-2).
https://sketchfab.com/3d-models/v-svz-term-p285-2ee5a21bde7d4232b9a4d00e4bcc545c
(Term P28.5).
https://sketchfab.com/3d-models/v-svz-preterm-p295-91d3f4b050184068b7513c8128c69f22
(Preterm P29.5).

ACKNOWLEDGMENTS

This work is dedicated to the memory of Prof. José Manuel García-Verdugo, who passed away after this paper was accepted. The authors are grateful to Ms. Maiko Tanaka, Mr. Akira Ito, Dr. Chikako Nakajima, Dr. Takuya Miyamoto, and Dr. Kazuya Kuboyama (Nagoya City University, Japan) for their assistance

and to other members of the Sawamoto laboratory for valuable discussions. We are grateful to Dr. Hiroshi Nomura and Ms. Nao Nomura for their valuable support in the creation of the 3D models. The authors thank Dr. Masatsugu Ema for providing *Flt1*-tdsRed mice; the CARD Mouse Bank at the Institute of Resource Development and Analysis, Kumamoto University, for providing C57BL/6-Tg(*Cdh5-Cre*^{ERT2}) mice; Dr. Masatoshi Takeichi and the Laboratory for Animal Resources and Genetic Engineering at the RIKEN Center for Biosystems Dynamics Research for providing *Cdh2*^{floxed} mice; Dr. Hiroyuki Miyoshi for providing plasmids; and Ms. Nobuko Hattori, Ms. Atsuko Imai, and the Section of Electron Microscopy at the National Institute for Physiological Sciences for their assistance with acquisition of SBF-SEM data. The authors also acknowledge the Center for Experimental Animal Science and the Core Laboratory at Nagoya City University for providing technical and animal support. The hybridomas producing the anti-CD31 (2H8) antibody, developed by Dr. Steven Bogen, were obtained from the Developmental Studies Hybridoma Bank (DSHB), developed under the auspices of the National Institute of Child Health and Human Development and maintained by the University of Iowa (Iowa City, IA, USA). Human tissue was obtained from the National Institutes of Health (NIH) NeuroBioBank under a materials transfer agreement with the NIH. The authors thank Dr. Susan Furness and Dr. Ryan Chastain-Gross from Edanz (https://jp.edanz.com/ac) and Dr. Elizabeth Nakajima for editing a draft of this manuscript. This work was supported by research grants from the Japan Agency for Medical Research and Development (AMED) (21bm0704033, 24gm1210007, and 25ym0126807 [to K.S.]), the Japan Society for the Promotion of Science (JSPS) KAKENHI (20H05700, 22H04925, 22H04926, 23H04939, 24H02016, 24K22003, 25H01040, and 25H02507 [to K.S.], 23K06321 [to S.T.], and 23K14983 [to K. Kawase]), Bilateral Open Partnership Joint Research Projects (to K.S.), the Core-to-Core Program "Neurogenesis Research & Innovation Center (NeuRIC)" (JPJSCCA20230007 [to K.S.]), a Grant-in-Aid for Promotion on Co-Creative Urban Development in Nagoya City University (2412145 to K.S.), a Grant-in-Aid for Outstanding Research Group Support Program in Nagoya City University (2401101 to K.S.), the Cooperative Study Programs of the National Institute for Physiological Sciences (to K.S.), the Takeda Science Foundation (to K.S.); the Mizutani Foundation (to K.S.), and the Valencian Council for Education, Culture, University and Employment (CIPROM/2023/053) to V.H.-P. and J.M.G.-V. Funding was also provided by Novo Nordisk Hallas-Møller Investigator grants (NNF16OC0019920 and NNF21OC0067146 [to K. Khodosevich]), the Lundbeckfonden Ascending Investigator grant (2020-1025 [to K. Khodosevich]), and the European Union's Horizon 2020 research and innovation program under the Marie Skłodowska-Curie grant agreement no. 801481 (to L.W.). This work used research equipment supported by the MEXT Project for Promoting Public Utilization of Advanced Research Infrastructure (program for supporting construction of core facilities; JPMXS0441500024).

AUTHOR CONTRIBUTIONS

S.T., K. Kawase, Y.N., M.M., H.J., A.T., and M.S. performed the experiments. S.T., K. Kawase, L.W., Y.N., M.M., H.J., A.T., M.S., V.H.-P., J.M.G.-V., N.I., V.G., N.O., K. Khodosevich, and K.S. analyzed the data. Y.K. provided resources. S.T., K. Kawase, L.W., and K.S. wrote the manuscript. All authors read and approved the final manuscript.

DECLARATION OF INTERESTS

The authors declare no competing interests.

STAR★METHODS

Detailed methods are provided in the online version of this paper and include the following:

- KEY RESOURCES TABLE
- EXPERIMENTAL MODEL AND STUDY PARTICIPANT DETAILS
  - Animals
  - Human specimens
- METHOD DETAILS
  - Mifepristone-induced preterm birth
  - Cesarean section-induced preterm birth
  - Progesterone-induced prolonged gestation
  - *In utero* surgeries
  - Viral vectors and plasmids and *in vivo* viral infection
  - Brain slices live imaging
  - Immunohistochemistry, confocal image acquisition and quantification
  - Western blotting
  - SBF-SEM
  - Single-cell isolation
  - 10× Genomics single-cell library preparation
  - Analysis of scRNA-seq data
  - Cell filtering
  - Sample integration and clustering
  - Expression of cell adhesion related genes
  - Differential gene expression analysis
  - Gene set enrichment analysis
- QUANTIFICATION AND STATISTICAL ANALYSIS

SUPPLEMENTAL INFORMATION

Supplemental information can be found online at https://doi.org/10.1016/j.celrep.2025.116029.

Received: May 13, 2024
Revised: April 14, 2025
Accepted: June 27, 2025

REFERENCES

1. Putnam, A.J. (2014). The Instructive Role of the Vasculature in Stem Cell Niches. Biomater. Sci. *2*, 1562–1573. https://doi.org/10.1039/C4BM00200H.
2. Genet, N., Genet, G., Chavkin, N.W., Paila, U., Fang, J.S., Vasavada, H.H., Goldberg, J.S., Acharya, B.R., Bhatt, N.S., Baker, K., et al. (2023). Connexin 43-mediated neurovascular interactions regulate neurogenesis in the adult brain subventricular zone. Cell Rep. *42*, 112371. https://doi.org/10.1016/J.CELREP.2023.112371.
3. Shen, Q., Wang, Y., Kokovay, E., Lin, G., Chuang, S.M., Goderie, S.K., Roysam, B., and Temple, S. (2008). Adult SVZ stem cells lie in a vascular niche: A quantitative analysis of niche cell-cell interactions. Cell Stem Cell *3*, 289–300. https://doi.org/10.1016/J.STEM.2008.07.026.
4. Tavazoie, M., Van der Veken, L., Silva-Vargas, V., Louissaint, M., Colonna, L., Zaidi, B., Garcia-Verdugo, J.M., and Doetsch, F. (2008). A Specialized Vascular Niche for Adult Neural Stem Cells. Cell Stem Cell *3*, 279–288. https://doi.org/10.1016/J.STEM.2008.07.025.
5. Palmer, T.D., Willhoite, A.R., and Gage, F.H. (2000). Rapid Publication Vascular Niche for Adult Hippocampal Neurogenesis. J. Comp. Neurol. *425*, 479–494. https://doi.org/10.1002/1096-9861.
6. Mirzadeh, Z., Merkle, F.T., Soriano-Navarro, M., Garcia-Verdugo, J.M., and Alvarez-Buylla, A. (2008). Neural stem cells confer unique pinwheel architecture to the ventricular surface in neurogenic regions of the adult brain. Cell Stem Cell *3*, 265–278. https://doi.org/10.1016/J.STEM.2008.07.004.
7. Fuentealba, L.C., Obernier, K., and Alvarez-Buylla, A. (2012). Adult Neural Stem Cells Bridge their Niche. Cell Stem Cell *10*, 698–708. https://doi.org/10.1016/J.STEM.2012.05.012.
8. Merkle, F.T., Tramontin, A.D., García-Verdugo, J.M., and Alvarez-Buylla, A. (2004). Radial glia give rise to adult neural stem cells in the subventricular zone. Proc. Natl. Acad. Sci. USA *101*, 17528–17532. https://doi.org/10.1073/PNAS.0407893101.
9. Kriegstein, A.R., and Götz, M. (2003). Radial glia diversity: A matter of cell fate. Glia *43*, 37–43. https://doi.org/10.1002/GLIA.10250.

Please cite this article in press as: Takemura et al., Transformation of radial glia into postnatal neural stem cells depends on birth, Cell Reports (2025), https://doi.org/10.1016/j.celrep.2025.116029

10. Kawase, K., Nakamura, Y., Wolbeck, L., Takemura, S., Zaitsu, K., Ando, T., Jinnou, H., Sawada, M., Nakajima, C., Rydbirk, R., et al. (2025). Significance of birth in the maintenance of quiescent neural stem cells. Sci. Adv. *11*, 6377. https://doi.org/10.1126/SCIADV.ADN6377.

11. Simon-Szabo, Z., Fogarasi, E., Nemes-Nagy, E., Denes, L., Croitoru, M., and Szabo, B. (2021). Oxidative stress and peripartum outcomes (Review). Exp. Ther. Med. *22*, 771. https://doi.org/10.3892/ETM.2021.10203.

12. Kanamori, T., Yoshino, J., Yasunaga, K.I., Dairyo, Y., and Emoto, K. (2015). Local endocytosis triggers dendritic thinning and pruning in Drosophila sensory neurons. Nat. Commun. *6*, 6515. https://doi.org/10.1038/ncomms7515.

13. Takeda, T., Kozai, T., Yang, H., Ishikuro, D., Seyama, K., Kumagai, Y., Abe, T., Yamada, H., Uchihashi, T., Ando, T., and Takei, K. (2018). Dynamic clustering of dynamin-amphiphysin helices regulates membrane constriction and fission coupled with GTP hydrolysis. eLife *7*, e30246. https://doi.org/10.7554/ELIFE.30246.

14. Mettlen, M., Chen, P.H., Srinivasan, S., Danuser, G., and Schmid, S.L. (2018). Regulation of Clathrin-Mediated Endocytosis. Annu. Rev. Biochem. *87*, 871–896. https://doi.org/10.1146/ANNUREV-BIOCHEM-062917-012644.

15. Kokovay, E., Wang, Y., Kusek, G., Wurster, R., Lederman, P., Lowry, N., Shen, Q., and Temple, S. (2012). VCAM1 is essential to maintain the structure of the SVZ niche and acts as an environmental sensor to regulate SVZ lineage progression. Cell Stem Cell *11*, 220–230. https://doi.org/10.1016/J.STEM.2012.06.016.

16. Morita, K., Sasaki, H., Furuse, M., and Tsukita, S. (1999). Endothelial Claudin: Claudin-5/Tmvcf Constitutes Tight Junction Strands in Endothelial Cells. J. Cell Biol. *147*, 185–194. https://doi.org/10.1083/JCB.147.1.185.

17. Gory-Fauré, S., Prandini, M.H., Pointu, H., Roullot, V., Pignot-Paintrand, I., Vernet, M., and Huber, P. (1999). Role of vascular endothelial-cadherin in vascular morphogenesis. Development *126*, 2093–2102. https://doi.org/10.1242/DEV.126.10.2093.

18. Porlan, E., Martí-Prado, B., Morante-Redolat, J.M., Consiglio, A., Delgado, A.C., Kypta, R., López-Otín, C., Kirstein, M., and Fariñas, I. (2014). MT5-MMP regulates adult neural stem cell functional quiescence through the cleavage of N-cadherin. Nat. Cell Biol. *16*, 629–638. https://doi.org/10.1038/ncb2993.

19. Dejana, E. (2004). Endothelial cell–cell junctions: happy together. Nat. Rev. Mol. Cell Biol. *5*, 261–270. https://doi.org/10.1038/nrm1357.

20. Gerhardt, H., Wolburg, H., and Redies, C. (2000). N-cadherin mediates pericytic-endothelial interaction during brain angiogenesis in the chicken. Dev. Dyn. *218*, 472–479. https://doi.org/10.1002/1097-0177(200007)218:3<472::AID-DVDY1008>3.0.CO;2.

21. Doetsch, F., García-Verdugo, J.M., and Alvarez-Buylla, A. (1997). Cellular Composition and Three-Dimensional Organization of the Subventricular Germinal Zone in the Adult Mammalian Brain. J. Neurosci. *17*, 5046–5061. https://doi.org/10.1523/JNEUROSCI.17-13-05046.1997.

22. Doetsch, F., Caillé, I., Lim, D.A., Manuel García-Verdugo, J., and Alvarez-Buylla, A. (1999). Subventricular Zone Astrocytes Are Neural Stem Cells in the Adult Mammalian Brain. Cell *97*, 703–716. https://doi.org/10.1016/s0092-8674(00)80783-7.

23. Alvarez-Buylla, A., and García-Verdugo, J.M. (2002). Neurogenesis in Adult Subventricular Zone. J. Neurosci. *22*, 629–634. https://doi.org/10.1523/JNEUROSCI.22-03-00629.2002.

24. Paredes, M.F., James, D., Gil-Perotin, S., Kim, H., Cotter, J.A., Ng, C., Sandoval, K., Rowitch, D.H., Xu, D., McQuillen, P.S., et al. (2016). Extensive migration of young neurons into the infant human frontal lobe. Science *354*, aaf7073. https://doi.org/10.1126/science.aaf7073.

25. Cebrian-Silla, A., Nascimento, M.A., Redmond, S.A., Mansky, B., Wu, D., Obernier, K., Romero Rodriguez, R., Gonzalez-Granero, S., García-Verdugo, J.M., Lim, D.A., and Álvarez-Buylla, A. (2021). Single-cell analysis of the ventricular-subventricular zone reveals signatures of dorsal and ventral adult neurogenic lineages. eLife *10*, e67436. https://doi.org/10.7554/ELIFE.67436.

26. Yaniv, S.P., and Schuldiner, O. (2016). A fly's view of neuronal remodeling. Wiley Interdiscip. Rev. Dev. Biol. *5*, 618–635. https://doi.org/10.1002/WDEV.241.

27. Noctor, S.C., Martínez-Cerdeño, V., Ivic, L., and Kriegstein, A.R. (2004). Cortical neurons arise in symmetric and asymmetric division zones and migrate through specific phases. Nat. Neurosci. *7*, 136–144. https://doi.org/10.1038/nn1172.

28. Lebouc, M., Richard, Q., Garret, M., and Baufreton, J. (2020). Striatal circuit development and its alterations in Huntington's disease. Neurobiol. Dis. *145*, 105076. https://doi.org/10.1016/J.NBD.2020.105076.

29. Kanamori, T., Kanai, M.I., Dairyo, Y., Yasunaga, K.I., Morikawa, R.K., and Emoto, K. (2013). Compartmentalized calcium transients trigger dendrite pruning in Drosophila sensory neurons. Science *340*, 1475–1478. https://doi.org/10.1126/SCIENCE.1234879.

30. Castillo-Badillo, J.A., Bandi, A.C., Harlalka, S., and Gautam, N. (2020). SRRF-Stream Imaging of Optogenetically Controlled Furrow Formation Shows Localized and Coordinated Endocytosis and Exocytosis Mediating Membrane Remodeling. ACS Synth. Biol. *9*, 902–919. https://doi.org/10.1021/ACSSYNBIO.9B00521.

31. Coleman, M. (2005). Axon degeneration mechanisms: commonality amid diversity. Nat. Rev. Neurosci. *6*, 889–898. https://doi.org/10.1038/nrn1788.

32. Ottone, C., Krusche, B., Whitby, A., Clements, M., Quadrato, G., Pitulescu, M.E., Adams, R.H., and Parrinello, S. (2014). Direct cell-cell contact with the vascular niche maintains quiescent neural stem cells. Nat. Cell Biol. *16*, 1045–1056. https://doi.org/10.1038/NCB3045.

33. Calì, C., Agus, M., Kare, K., Boges, D.J., Lehväslaiho, H., Hadwiger, M., and Magistretti, P.J. (2019). 3D cellular reconstruction of cortical glia and parenchymal morphometric analysis from Serial Block-Face Electron Microscopy of juvenile rat. Prog. Neurobiol. *183*, 101696. https://doi.org/10.1016/J.PNEUROBIO.2019.101696.

34. Kawaguchi, D., Furutachi, S., Kawai, H., Hozumi, K., and Gotoh, Y. (2013). Dll1 maintains quiescence of adult neural stem cells and segregates asymmetrically during mitosis. Nat. Commun. *4*, 1880. https://doi.org/10.1038/ncomms2895.

35. Myshrall, T.D., Moore, S.A., Ostendorf, A.P., Satz, J.S., Kowalczyk, T., Nguyen, H., Daza, R.A.M., Lau, C., Campbell, K.P., and Hevner, R.F. (2012). Dystroglycan on radial glia end feet is required for pial basement membrane integrity and columnar organization of the developing cerebral cortex. J. Neuropathol. Exp. Neurol. *71*, 1047–1063. https://doi.org/10.1097/NEN.0B013E318274A128.

36. Wolburg, H., Noell, S., Mack, A., Wolburg-Buchholz, K., and Fallier-Becker, P. (2008). Brain endothelial cells and the glio-vascular complex. Cell Tissue Res. *335*, 75–96. https://doi.org/10.1007/S00441-008-0658-9.

37. McClenahan, F.K., Sharma, H., Shan, X., Eyermann, C., and Colognato, H. (2016). Dystroglycan suppresses Notch to regulate stem cell niche structure and function in the developing postnatal subventricular zone. Dev. Cell *38*, 548–566. https://doi.org/10.1016/J.DEVCEL.2016.07.017.

38. Simon, M.C., and Keith, B. (2008). The role of oxygen availability in embryonic development and stem cell function. Nat. Rev. Mol. Cell Biol. *9*, 285–296. https://doi.org/10.1038/NRM2354.

39. Puente, B.N., Kimura, W., Muralidhar, S.A., Moon, J., Amatruda, J.F., Phelps, K.L., Grinsfelder, D., Rothermel, B.A., Chen, R., Garcia, J.A., et al. (2014). The Oxygen-Rich Postnatal Environment Induces Cardiomyocyte Cell-Cycle Arrest through DNA Damage Response. Cell *157*, 565–579. https://doi.org/10.1016/J.CELL.2014.03.032.

40. Jurisch-Yaksi, N., Yaksi, E., and Kizil, C. (2020). Radial glia in the zebrafish brain: Functional, structural, and physiological comparison with the mammalian glia. Glia *68*, 2451–2470. https://doi.org/10.1002/GLIA.23849.

41. Scatliffe, N., Casavant, S., Vittner, D., and Cong, X. (2019). Oxytocin and early parent-infant interactions: A systematic review. Int. J. Nurs. Sci. *6*, 445–453. https://doi.org/10.1016/J.IJNSS.2019.09.009.

42. Tyzio, R., Cossart, R., Khalilov, I., Minlebaev, M., Hübner, C.A., Represa, A., Ben-Ari, Y., and Khazipov, R. (2006). Maternal oxytocin triggers a transient

Please cite this article in press as: Takemura et al., Transformation of radial glia into postnatal neural stem cells depends on birth, Cell Reports (2025), https://doi.org/10.1016/j.celrep.2025.116029

inhibitory switch in GABA signaling in the fetal brain during delivery. Science *314*, 1788–1792. https://doi.org/10.1126/SCIENCE.1133212.

43. Di Scala-Guenot, D., Mouginot, D., and Strosser, M.-T. (1994). Increase of intracellular calcium induced by oxytocin in hypothalamic cultured astrocytes. Glia *11*, 269–276. https://doi.org/10.1002/GLIA.440110308.
44. Ami, O., Maran, J.C., Gabor, P., Whitacre, E.B., Musset, D., Dubray, C., Mage, G., and Boyer, L. (2019). Three-dimensional magnetic resonance imaging of fetal head molding and brain shape changes during the second stage of labor. PLoS One *14*, e0215721. https://doi.org/10.1371/JOURNAL.PONE.0215721.
45. Kilinc, D., Gallo, G., and Barbee, K.A. (2009). Mechanical membrane injury induces axonal beading through localized activation of calpain. Exp. Neurol. *219*, 553–561. https://doi.org/10.1016/J.EXPNEUROL.2009.07.014.
46. Hara, Y., Kumamoto, T., Yoshizawa-Sugata, N., Hirai, K., Song, X., Kawaji, H., and Ohtaka-Maruyama, C. (2025). The spatial transcriptome of the late-stage embryonic and postnatal mouse brain reveals spatiotemporal molecular markers. Sci. Rep. *15*, 12299. https://doi.org/10.1038/s41598-025-95496-8.
47. Nowakowski, T.J., Pollen, A.A., Sandoval-Espinosa, C., and Kriegstein, A.R. (2016). Transformation of the Radial Glia Scaffold Demarcates Two Stages of Human Cerebral Cortex Development. Neuron *91*, 1219–1227. https://doi.org/10.1016/j.neuron.2016.09.005.
48. Bilgic, M., Wu, Q., Suetsugu, T., Shitamukai, A., Tsunekawa, Y., Shimogori, T., Kadota, M., Nishimura, O., Kuraku, S., Kiyonari, H., and Matsuzaki, F. (2023). Truncated radial glia as a common precursor in the late corticogenesis of gyrencephalic mammals. eLife *12*, RP91406. https://doi.org/10.7554/ELIFE.91406.3.
49. Clancy, B., Darlington, R.B., and Finlay, B.L. (2001). Translating developmental time across mammalian species. Neuroscience *105*, 7–17. https://doi.org/10.1016/S0306-4522(01)00171-3.
50. Spong, C.Y. (2013). Defining "Term" Pregnancy: Recommendations From the Defining "Term" Pregnancy Workgroup. JAMA *309*, 2445–2446. https://doi.org/10.1001/JAMA.2013.6235.
51. Qiu, C., Martin, B.K., Welsh, I.C., Daza, R.M., Le, T.M., Huang, X., Nichols, E.K., Taylor, M.L., Fulton, O., O'Day, D.R., et al. (2024). A single-cell time-lapse of mouse prenatal development from gastrula to birth. Nature *626*, 1084–1093. https://doi.org/10.1038/S41586-024-07069-W.
52. Schaeffer, S., and Iadecola, C. (2021). Revisiting the neurovascular unit. Nat. Neurosci. *24*, 1198–1209. https://doi.org/10.1038/s41593-021-00904-7.
53. Shingo, T., Gregg, C., Enwere, E., Fujikawa, H., Hassam, R., Geary, C., Cross, J.C., and Weiss, S. (2003). Pregnancy-stimulated neurogenesis in the adult female forebrain mediated by prolactin. Science *299*, 117–120. https://doi.org/10.1126/SCIENCE.1076647.
54. Tsai, P.T., Ohab, J.J., Kertesz, N., Groszer, M., Matter, C., Gao, J., Liu, X., Wu, H., and Carmichael, S.T. (2006). A Critical Role of Erythropoietin Receptor in Neurogenesis and Post-Stroke Recovery. J. Neurosci. *26*, 1269–1274. https://doi.org/10.1523/JNEUROSCI.4480-05.2006.
55. Sawada, M., Ohno, N., Kawaguchi, M., Huang, S.H., Hikita, T., Sakurai, Y., Bang Nguyen, H., Quynh Thai, T., Ishido, Y., Yoshida, Y., et al. (2018). PlexinD1 signaling controls morphological changes and migration termination in newborn neurons. EMBO J. *37*, e97404. https://doi.org/10.15252/embj.201797404.
56. Jinnou, H., Sawada, M., Kawase, K., Kaneko, N., Herranz-Pérez, V., Miyamoto, T., Kawaue, T., Miyata, T., Tabata, Y., Akaike, T., et al. (2018). Radial Glial Fibers Promote Neuronal Migration and Functional Recovery after Neonatal Brain Injury. Cell Stem Cell *22*, 128–137.e9. https://doi.org/10.1016/j.stem.2017.11.005.
57. Matsumoto, K., Azami, T., Otsu, A., Takase, H., Ishitobi, H., Tanaka, J., Miwa, Y., Takahashi, S., and Ema, M. (2012). Study of normal and pathological blood vessel morphogenesis in Flt1-tdsRed BAC Tg mice. Genesis *50*, 561–571. https://doi.org/10.1002/DVG.22031.
58. Malvin, N.P., Seno, H., and Stappenbeck, T.S. (2012). Colonic epithelial response to injury requires Myd88 signaling in myeloid cells. Mucosal Immunol. *5*, 194. https://doi.org/10.1038/MI.2011.65.
59. Ota, H., Hikita, T., Sawada, M., Nishioka, T., Matsumoto, M., Komura, M., Ohno, A., Kamiya, Y., Miyamoto, T., Asai, N., et al. (2014). Speed control for neuronal migration in the postnatal brain by Gmip-mediated local inactivation of RhoA. Nat. Commun. 1–12. https://doi.org/10.1038/ncomms5532.
60. Berger, D.R., Seung, H.S., and Lichtman, J.W. (2018). VAST (Volume Annotation and Segmentation Tool): Efficient manual and semi-automatic labeling of large 3D image stacks. Front. Neural Circuits *12*, 406276. https://doi.org/10.3389/FNCIR.2018.00088.
61. Belevich, I., Joensuu, M., Kumar, D., Vihinen, H., and Jokitalo, E. (2016). Microscopy Image Browser: A Platform for Segmentation and Analysis of Multidimensional Datasets. PLoS Biol. *14*, e1002340. https://doi.org/10.1371/JOURNAL.PBIO.1002340.
62. Kick, F.L., Holze, H., Rydbirk, R., and Khodosevich, K. (2023). CRMetrics - an R package for Cell Ranger Filtering and Metrics Visualisation. Res Sq. https://doi.org/10.21203/RS.3.RS-2853524/V1.
63. Wolock, S.L., Lopez, R., and Klein, A.M. (2019). Scrublet: Computational Identification of Cell Doublets in Single-Cell Transcriptomic Data. Cell Syst. *8*, 281–291.e9. https://doi.org/10.1016/J.CELS.2018.11.005.
64. Barkas, N., Petukhov, V., Nikolaeva, D., Lozinsky, Y., Demharter, S., Khodosevich, K., and Kharchenko, P.V. (2019). Joint analysis of heterogeneous single-cell RNA-seq dataset collections. Nat. Methods *16*, 695–698. https://doi.org/10.1038/s41592-019-0466-z.
65. Petukhov, V., Igolkina, A., Rydbirk, R., Mei, S., Christoffersen, L., Khodosevich, K., and Kharchenko, P.V. (2022). Case-control analysis of single-cell RNA-seq studies. Preprint at bioRxiv. https://doi.org/10.1101/2022.03.15.484475.
66. Okabe, K., Kobayashi, S., Yamada, T., Kurihara, T., Tai-Nagara, I., Miyamoto, T., Mukouyama, Y.S., Sato, T.N., Suda, T., Ema, M., and Kubota, Y. (2014). Neurons limit angiogenesis by titrating VEGF in retina. Cell *159*, 584–596. https://doi.org/10.1016/J.CELL.2014.09.025.
67. Dudley, D.J., Branch, D.W., Edwin, S.S., and Mitchell, M.D. (1996). Induction of preterm birth in mice by RU486. Biol. Reprod. *55*, 992–995. https://doi.org/10.1095/biolreprod55.5.992.
68. Toda, T., Homma, D., Tokuoka, H., Hayakawa, I., Sugimoto, Y., Ichinose, H., and Kawasaki, H. (2013). Birth regulates the initiation of sensory map formation through serotonin signaling. Dev. Cell *27*, 32–46. https://doi.org/10.1016/j.devcel.2013.09.002.
69. Baulieu, E.E. (1989). Contragestion and other clinical applications of RU 486, an antiprogesterone at the receptor. Science *245*, 1351–1357. https://doi.org/10.1126/SCIENCE.2781282.
70. Morais, L.H., Golubeva, A.V., Moloney, G.M., Moya-Pérez, A., Ventura-Silva, A.P., Arboleya, S., Bastiaanssen, T.F.S., O'Sullivan, O., Rea, K., Borre, Y., et al. (2020). Enduring Behavioral Effects Induced by Birth by Caesarean Section in the Mouse. Curr. Biol. *30*, 3761–3774.e6. https://doi.org/10.1016/J.CUB.2020.07.044.
71. Rahman, A., Cahill, L.S., Zhou, Y.Q., Hoggarth, J., Rennie, M.Y., Seed, M., Macgowan, C.K., Kingdom, J.C., Adamson, S.L., and Sled, J.G. (2017). A mouse model of antepartum stillbirth. Am. J. Obstet. Gynecol. *217*, 443.e1–443.e11. https://doi.org/10.1016/J.AJOG.2017.06.009.
72. Figueres-Oñate, M., García-Marqués, J., Pedraza, M., De Carlos, J.A., and López-Mascaraque, L. (2015). Spatiotemporal analyses of neural lineages after embryonic and postnatal progenitor targeting combining different reporters. Front. Neurosci. *9*, 129862. https://doi.org/10.3389/FNINS.2015.00087.
73. Rust, R., Kirabali, T., Grönnert, L., Dogancay, B., Limasale, Y.D.P., Meinhardt, A., Werner, C., Laviña, B., Kulic, L., Nitsch, R.M., et al. (2020). A Practical Guide to the Automated Analysis of Vascular Growth, Maturation and Injury in the Brain. Front. Neurosci. *14*, 511979. https://doi.org/10.3389/FNINS.2020.00244.

Please cite this article in press as: Takemura et al., Transformation of radial glia into postnatal neural stem cells depends on birth, Cell Reports (2025), https://doi.org/10.1016/j.celrep.2025.116029

74. Thai, T.Q., Nguyen, H.B., Saitoh, S., Wu, B., Saitoh, Y., Shimo, S., Elewa, Y.H.A., Ichii, O., Kon, Y., Takaki, T., et al. (2016). Rapid specimen preparation to improve the throughput of electron microscopic volume imaging for three-dimensional analyses of subcellular ultrastructures with serial block-face scanning electron microscopy. Med. Mol. Morphol. *49*, 154–162. https://doi.org/10.1007/S00795-016-0134-7.

75. Nguyen, H.B., Thai, T.Q., Saitoh, S., Wu, B., Saitoh, Y., Shimo, S., Fujitani, H., Otobe, H., and Ohno, N. (2016). Conductive resins improve charging and resolution of acquired images in electron microscopic volume imaging. Sci. Rep. *6*, 23721. https://doi.org/10.1038/srep23721.

76. Matsumoto, M., Sawada, M., García-González, D., Herranz-Pérez, V., Ogino, T., Nguyen, H.B., Thai, T.Q., Narita, K., Kumamoto, N., Ugawa, S., et al. (2019). Dynamic Changes in Ultrastructure of the Primary Cilium in Migrating Neuroblasts in the Postnatal Brain. J. Neurosci. *39*, 9967–9988. https://doi.org/10.1523/JNEUROSCI.1503-19.2019.

77. Kurematsu, C., Sawada, M., Ohmuraya, M., Tanaka, M., Kuboyama, K., Ogino, T., Matsumoto, M., Oishi, H., Inada, H., Ishido, Y., et al. (2022). Synaptic pruning of murine adult-born neurons by microglia depends on phosphatidylserine. J. Exp. Med. *219*, e20202304. https://doi.org/10.1084/JEM.20202304/213073.

78. Kaneko, N., Herranz-Pérez, V., Otsuka, T., Sano, H., Ohno, N., Omata, T., Nguyen, H.B., Thai, T.Q., Nambu, A., Kawaguchi, Y., et al. (2018). New neurons use slit-robo signaling to migrate through the glial meshwork and approach a lesion for functional regeneration. Sci. Adv. *4*, eaav0618. https://doi.org/10.1126/SCIADV.AAV0618.

79. Mirzadeh, Z., Doetsch, F., Sawamoto, K., Wichterle, H., and Alvarez-Buylla, A. (2010). The subventricular zone en-face: wholemount staining and ependymal flow. J. Vis. Exp. 1938. https://doi.org/10.3791/1938.

80. Batiuk, M.Y., Tyler, T., Dragicevic, K., Mei, S., Rydbirk, R., Petukhov, V., Deviatiiarov, R., Sedmak, D., Frank, E., Feher, V., et al. (2022). Upper cortical layer–driven network impairment in schizophrenia. Sci. Adv. *8*, eabn8367. https://doi.org/10.1126/SCIADV.ABN8367.

81. Wu, T., Hu, E., Xu, S., Chen, M., Guo, P., Dai, Z., Feng, T., Zhou, L., Tang, W., Zhan, L., et al. (2021). clusterProfiler 4.0: A universal enrichment tool for interpreting omics data. Innovation *2*, 100141. https://doi.org/10.1016/J.XINN.2021.100141.

82. Yu, G. (2022). enrichplot: Visualization of Functional Enrichment Result; https://yulab-smu.top/biomedical-knowledge-mining-book/. R package version 1.18.3.

Please cite this article in press as: Takemura et al., Transformation of radial glia into postnatal neural stem cells depends on birth, Cell Reports (2025), https://doi.org/10.1016/j.celrep.2025.116029

STAR★METHODS

KEY RESOURCES TABLE

REAGENT or RESOURCE	SOURCE	IDENTIFIER
Antibodies		
Armenian hamster anti-CD31	DSHB	Cat# 2H8, RRID:AB_2161039
Chicken anti-Nestin	Aves Labs	Cat#NES; RRID: AB_2314882
Chicken anti-glial fibrillary acidic protein (GFAP)	Abcam	Cat# ab4674, RRID:AB_304558
Chicken anti-RFP	Rockland	Cat# 600-901-379S, RRID:AB_10703148
Chicken anti-Vimentin	Millipore	Cat# AB5733; RRID:AB_11212377
Mouse anti-Mash1	Santa Cruz Biotechnology	Cat# sc-374104, RRID:AB_1091856
Mouse anti-N-Cadherin	BD Biosciences	Cat#610921; RRID: AB_398236
Mouse anti-α-Actin	Santa Cruz Biotechnology	Cat# sc-32251, RRID:AB_262054
Mouse anti-epidermal growth factor receptor (EGFR)	Santa Cruz Biotechnology	Cat# sc-373746, RRID:AB_10920395
Mouse anti-Clathrin HC	Santa Cruz Biotechnology	Cat# sc-271178, RRID:AB_10610951
Mouse anti-β-Actin	Sigma-Aldrich	Cat# A2228, RRID:AB_476697
Rabbit anti-GFP	MBL International	Cat# JM-3999-100, RRID:AB_591818
Rabbit anti-DsRed	Takara	Cat# 632496, RRID:AB_10013483
Rabbit anti-N-Cadherin	Abcam	Cat# ab76011, RRID:AB_1310479
Rabbit anti-Mfsd2a	Cell Signaling Technology	Cat# 80302, RRID: N/A
Rabbit anti-Doublecortin	Cell Signaling Technology	Cat#4604; RRID: AB_561007
Rat anti-GFP	Nacalai Tesque	Cat#04404-84; RRID: AB_10013361
Alexa Fluor 405 donkey anti-chicken IgG (H+L)	Abcam	Cat# ab175675, RRID:AB_2810980
Alexa Fluor 405 donkey anti-mouse IgG (H+L)	Abcam	Cat# ab175658, RRID:AB_2687445
Alexa Fluor 405 donkey anti-rabbit IgG (H+L)	Abcam	Cat# ab175649, RRID:AB_2715515
Alexa Fluor 488 donkey anti-chicken IgY (H+L)	Invitrogen	Cat# A78948, RRID:AB_2921070
Alexa Fluor 488 donkey anti-mouse IgG (H+L)	Invitrogen	Cat#A21202; RRID: AB_141607
Alexa Fluor 488 donkey anti-rabbit IgG (H+L)	Invitrogen	Cat#A21206; RRID: AB_141708
Alexa Fluor 488 donkey anti-rat IgG (H+L)	Invitrogen	Cat#A21208; RRID: AB_141709
Alexa Fluor 568 donkey anti-mouse IgG (H+L)	Invitrogen	Cat#A10037; RRID: AB_2534013
Alexa Fluor 568 donkey anti-rabbit IgG (H+L)	Invitrogen	Cat#A10042; RRID: AB_2534017
Alexa Fluor 647 donkey anti-mouse IgG (H+L)	Invitrogen	Cat#A31571; RRID: AB_162542
Alexa Fluor 647 donkey anti-rabbit IgG (H+L)	Invitrogen	Cat#A31573; RRID: AB_2536183
Cy2-AffiniPure donkey anti-chicken IgY (IgG) (H+L)	Jackson ImmunoResearch	Cat#703-225-155; RRID: AB_2340370
Cy3-AffiniPure donkey anti-chicken IgY (IgG) (H+L)	Jackson ImmunoResearch	Cat#703-165-155; RRID: AB_2340363
Cy5-AffiniPure donkey anti-chicken IgY (IgG) (H+L)	Jackson ImmunoResearch	Cat#703-175-155; RRID: AB_2340365
Peroxidase-AffiniPure Donkey Anti-Mouse IgG (H+L)	Jackson ImmunoResearch	Cat# 715-035-151, RRID:AB_2340771
AffiniPure Fab Fragment Donkey anti-Mouse IgG (H+L)	Jackson ImmunoResearch	Cat#715-007-003; RRID: AB_2307338
Biotin-SP-AffiniPure F(ab')2 Fragment Donkey Anti-Rabbit IgG (H + L)	Jackson ImmunoResearch	Cat# 711-066-152; RRID:AB_2340594
Hoechst 33342	Thermo Fisher Scientific	Cat#62249
Vectashield	Vector Laboratories	Cat# H-1700; RRID:N/A
Bacterial and virus strains		
CSII-EF-EmGFP-CAAX-miR-LacZ	Sawada et al.[55]	N/A
CSII-EF-EmGFP-CAAX-miR-Cdh2	Jinnou et al.[56]	N/A
CSII-EF-EmGFP-CAAX-miR-Cltc	This paper	N/A
CSII-hGFAP-tdTomato-CAAX	This paper	N/A

(*Continued on next page*)

Please cite this article in press as: Takemura et al., Transformation of radial glia into postnatal neural stem cells depends on birth, Cell Reports (2025), https://doi.org/10.1016/j.celrep.2025.116029

Continued

REAGENT or RESOURCE	SOURCE	IDENTIFIER
Biological samples		
Human brain tissue: term, male, gestational age at birth: 39 weeks, age at death: 42 days, corrected gestational age at death: 45 weeks, postmortem interval: 21 hours, cause of death: sudden unexplained infant death	NIH NeuroBioBank	N/A
Human brain tissue: term, male, gestational age at birth: 37 weeks, age at death: 28 days, corrected gestational age at death: 41 weeks, postmortem interval: 34 hours, cause of death: sudden unexplained infant death	NIH NeuroBioBank	N/A
Human brain tissue: term, female, gestational age at birth: 40 weeks, age at death: 54 days, corrected gestational age at death: 48 weeks, postmortem interval: 34 hours, cause of death: sudden unexplained infant death	NIH NeuroBioBank	N/A
Human brain tissue: preterm, female, gestational age at birth: 26 weeks, age at death: 142 days, corrected gestational age at death: 46 weeks, postmortem interval: 27 hours, cause of death: suffocation by pillow	NIH NeuroBioBank	N/A
Human brain tissue: preterm, male, gestational age at birth: 33 weeks, age at death: 149 days, corrected gestational age at death: 54 weeks, postmortem interval: 13 hours, cause of death: sudden unexplained infant death	NIH NeuroBioBank	N/A
Human brain tissue: preterm, male, gestational age at birth: 34 weeks, age at death: 99 days, corrected gestational age at death: 48 weeks, postmortem interval: 33 hours, cause of death: sudden unexplained infant death	NIH NeuroBioBank	N/A
Chemicals, peptides, and recombinant proteins		
Tamoxifen	Sigma-Aldrich	Cat# T5648
Corn Oil	Sigma-Aldrich	Cat# C8267
Mifepristone	Sigma-Aldrich	Cat# M8046
Isoflurane	Viatris	VTRS
Medroxyprogesterone 17-acetate	Sigma-Aldrich	Cat# M1629
Calpain inhibitor III	Bachem	Cat# 4027129.0025
MiTMAB	Sigma-Aldrich	Cat# T4762
Blocking reagent	Akoya Biosciences	Cat# FP1012
VECTASHIELD mounting medium with DAPI	Vector Laboratories	Cat# H-1200; RRID:AB_2336790
TSA Plus Cyanine 3 Kit	Akoya Biosciences	Cat# NEL744001KT
Streptavidin-HRP	Akoya Biosciences	Cat# NEL750001EA; RRID:AB_2617185
Fast green	Sigma-Aldrich	Cat# F7252
Normal donkey serum	Millipore	Cat# S30-100ML
Protease inhibitor cocktail	Nacalai Tesque	03969-21
Bio-Rad Protein Assay	Bio-Rad	Cat# 500-0006
Skim milk	Wako	Cat# 190-12865
Neurobasal medium	Gibco	Cat# 21103-049
Fetal Bovine Serum	Gibco	Cat# 10437
NeuroBrew-21	Miltenyi Biotec	Cat# 130-093-566
Glutamax	Gibco	Cat# 35050-061
Antibiotic-Antimycotic	Gibco	Cat# 15240-062
Papain-EBSS	Worthington	Cat# LK003150
RNase-free PBS	Invitrogen	Cat# AM9624
RNase inhibitor	Thermofisher	Cat# N8080119
Trypan blue	Thermofisher	Cat# 15250061

(*Continued on next page*)

Please cite this article in press as: Takemura et al., Transformation of radial glia into postnatal neural stem cells depends on birth, Cell Reports (2025), https://doi.org/10.1016/j.celrep.2025.116029

Continued

REAGENT or RESOURCE	SOURCE	IDENTIFIER
Critical commercial assays		
PureLink HiPure Plasmid Midiiprep Kit	Invitrogen	Cat# K2100-04
PureLink HiPure Plasmid Maxiprep Kit	Invitrogen	Cat# K2100-06
Block-iT Pol II miR RNAi entry vector containing EmGFP	Thermofisher	Cat# K493500
pENTR™/D-TOPO™ Cloning Kit, Thermofisher	Thermofisher	Cat# K240020SP
Gateway™ LR Clonase™ II Enzyme mix	Thermofisher	Cat# 11791100
Amersham ECL Prime Western Blotting Detection Reagent	Cytiva	Cat# RPN2232
AnaeroPack Bikouki	Mitsubishi Gas Chemical	Cat# A-28
Chromium Single Cell 3′ v3.1	10x Genomics	Cat# PN-1000128
Deposited data		
scRNA-seq dataset: E18.5, Term P2.5, Preterm P0.5, Preterm P3.5)	Kawase et al.[10]; the Sequence Read Archive, NCBI	https://www.ncbi.nlm.nih.gov/sra/PRJNA944115
scRNA-seq dataset: Term P28.5, Preterm P29.5	This paper	https://www.ncbi.nlm.nih.gov/sra/PRJNA1073531
Experimental models: Organisms/strains		
Mouse: ICR	Japan SLC	N/A
Mouse: C57BL6/J	Japan SLC	N/A
Mouse: GFAP-EGFP	Mutant Mouse Regional Resource Center	Stock No. 000315-MU
Mouse: Flt1-tdsRed	Matsumoto et al.[57], Gift from Dr. Masatsugu Ema	N/A
Mouse: *Cdh2^{floxed}*	Gift from Dr. Masatoshi Takeichi	N/A
Mouse: C57BL/6-Tg(*Cdh5-Cre^{ERT2}*)	CARD Mouse Bank	CARD ID: 2361
Human brain tissue: term, male, gestational age at birth: 39 weeks, age at death: 42 days, corrected gestational age at death: 45 weeks, postmortem interval: 21 hours, cause of death: sudden unexplained infant death	NIH NeuroBioBank	N/A
Human brain tissue: term, male, gestational age at birth: 37 weeks, age at death: 28 days, corrected gestational age at death: 41 weeks, postmortem interval: 34 hours, cause of death: sudden unexplained infant death	NIH NeuroBioBank	N/A
Human brain tissue: term, female, gestational age at birth: 40 weeks, age at death: 54 days, corrected gestational age at death: 48 weeks, postmortem interval: 34 hours, cause of death: sudden unexplained infant death	NIH NeuroBioBank	N/A
Human brain tissue: preterm, female, gestational age at birth: 26 weeks, age at death: 142 days, corrected gestational age at death: 46 weeks, postmortem interval: 27 hours, cause of death: suffocation by pillow	NIH NeuroBioBank	N/A
Human brain tissue: preterm, male, gestational age at birth: 33 weeks, age at death: 149 days, corrected gestational age at death: 54 weeks, postmortem interval: 13 hours, cause of death: sudden unexplained infant death	NIH NeuroBioBank	N/A
Human brain tissue: preterm, male, gestational age at birth: 34 weeks, age at death: 99 days, corrected gestational age at death: 48 weeks, postmortem interval: 33 hours, cause of death: sudden unexplained infant death	NIH NeuroBioBank	N/A
Experimental models: Cell lines		
HEK293T		RRID:CVCL_0063
Neuro2A		RRID:CVCL_0470

(*Continued on next page*)

Please cite this article in press as: Takemura et al., Transformation of radial glia into postnatal neural stem cells depends on birth, Cell Reports (2025), https://doi.org/10.1016/j.celrep.2025.116029

Continued

REAGENT or RESOURCE	SOURCE	IDENTIFIER
Oligonucleotides		
miR-LacZ (657) forward primer: 5'-TGCTGAAATCGCTG ATTTGTGTAGTCGTTTTGGCCACTGACTGACGACTAC ACATCAGCGATTT-3'	Sawada et al.[55]	N/A
miR-LacZ (657) reverse primer: 5'-CCTGAAATCGCTGA TGTGTAGTCGTCAGTCAGTGGCCAAAACGACTACACA AATCAGCGATTTC-3'	Sawada et al.[55]	N/A
miR-Cdh2 (944) forward primer: 5'-TGCTGTAAACA TGTTGGGTGAAGGTGGTTTTGGCCACTGACTGA CCACCTTCACAACATGTTTA-3'	Jinnou et al.[56]	N/A
miR-Cdh2 (944) reverse primer: 5'-CCTGTAAACAT GTTGTGAAGGTGGTCAGTCAGTGGCCAAAACCA CCTTCACCCAACATGTTTAC-3'	Jinnou et al.[56]	N/A
miR-Cltc (4464) forward primer: 5'-TGCTGTGTAGG AGCTCTTCAGCCAATGTTTTGGCCACTGACTGAC ATTGGCTGGAGCTCCTACA-3'	This paper	N/A
miR-Cltc (4464) reverse primer: 5'-CCTGTGTAGGA GCTCCAGCCAATGTCAGTCAGTGGCCAAAACATT GGCTGAAGAGCTCCTACAC-3'	This paper	N/A
Genotyping primer for *Cdh2 floxed* (forward): 5'-CC AAAGCTGAGTGTGACTTG-3'	Jackson Laboratory	N/A
Genotyping primer for *Cdh2 floxed* (reverse): 5'-TA CAAGTTTGGGTGACAAGC-3'	Jackson Laboratory	N/A
Genotyping primer for *Cdh5-CreERT2* (Cre; forward): 5'-AGGTTCGTTCACTCATGGA-3'	Malvin et al.[58]	N/A
Genotyping primer for *Cdh5-CreERT2* (Cre; reverse): 5′-TCGACCAGTTTAGTTACC C-3′	Malvin et al.[58]	N/A
Recombinant DNA		
pCAGGS-EmGFP-miR-LacZ	Ota et al.[59]	N/A
pCAG-HIVgp		N/A
pCMV-VSV-G-RSV-Rev		N/A
hGFAP-Cre	Addgene	Plasmid #40591
CSII-EF-RfA-IRES2-Venus	from Dr. Hiroyuki Miyoshi, RIKEN	Cat#RDB04389
CSII-EF-EmGFP-CAAX-miR-LacZ	Sawada et al.[55]	N/A
CSII-EF-EmGFP-CAAX-miR-Cdh2	Jinnou et al.[56]	N/A
CSII-EF-EmGFP-CAAX-miR-Cltc	This paper	N/A
CSII-hGFAP-tdTomato-CAAX	This paper	N/A
Software and algorithms		
BLOCK-iT RNAi Designer	Thermo Fisher	https://rnaidesigner.thermofisher.com/rnaiexpress/
FIJI (ImageJ)	National Institutes of Health	https://imagej.nih.gov/ij/
Neurolucida	MBF Bioscience	http://www.mbfbioscience.com/neurolucida
CellSens	Evident	
ZEN	Carl Zeiss	https://www.zeiss.com/microscopy/int/products/microscope-software/zen.html
Volume Annotation and Segmentation Tool Lite	Berger et al.[60]	https://lichtman.rc.fas.harvard.edu/vast/
Microscopy Image Browser	Belevich et al.[61]	https://mib.helsinki.fi/
Amira software (6.2.0, 2020.2)	Thermo Fisher	
Blender	N/A	https://www.blender.org
Sketchfab	N/A	https://sketchfab.com

(*Continued on next page*)

Please cite this article in press as: Takemura et al., Transformation of radial glia into postnatal neural stem cells depends on birth, Cell Reports (2025), https://doi.org/10.1016/j.celrep.2025.116029

Continued

REAGENT or RESOURCE	SOURCE	IDENTIFIER
Cell Ranger v5.0.0	10x Genomics	N/A
R package CRMetrics v0.2.3	Kick et al.[62]	https://github.com/khodosevichlab/CRMetrics/blob/main/README.md
Scrublet	Wolock et al.[63]	N/A
Pagoda2	N/A	https://github.com/kharchenkolab/pagoda2
Conos	Barkas et al.[64]	https://github.com/kharchenkolab/conos
Cacoa	Petukhov et al.[65]	https://github.com/kharchenkolab/cacoa
GraphPad Prism 10	GraphPad Software	https://www.graphpad.com/
Other		
Electroporator	NepaGene	NEPA21
Wiretrol I (5 μl)	Drummond Scientific Company	Cat#5-000-1005
Stereotaxic injection apparatus	David Kopf Instruments	N/A
Immobilon-P membrane PVDF	Millipore	Cat# IPVH00010
ImageQuant LAS 4000 mini	Cytiva	N/A
Millicell inserts	Millipore	PICM0RG50
Glass-bottom dishes	Matsunami	D11140H
Stage-top chamber	Tokai Hit	Model: STXG-WSBX-SET
Cell strainer 40 μm	BD Falcon	352340
Cell strainer 70 μm	BD Falcon	352350
FV1000 microscope	Evident	N/A
FV3000 microscope	Evident	N/A
LSM880 microscope	Carl Zeiss	N/A
Merlin scanning electron microscope	Carl Zeiss	N/A
Sigma scanning electron microscope	Carl Zeiss	N/A
3View in-chamber ultramicrotome system	Gatan	N/A
Chromium Next GEM Chip G	10x Genomics	Cat# PN-2000177
NovaSeq 6000 platform	Illumina	N/A

EXPERIMENTAL MODEL AND STUDY PARTICIPANT DETAILS

Animals

Wild-type (WT) Institute for Cancer Research (ICR) and C57BL6/J mice were purchased from Japan SLC. *GFAP-EGFP* mice were obtained from the Mutant Mouse Regional Resource Center (MMRRC, Stock No. 000315-MU) and maintained on an ICR genetic background. *Flt1-tdsRed* mice[57] were a gift from Dr. Masatsugu Ema maintained by crossing heterozygote males with WT C57BL6/J females. *Cdh2*^{floxed} mice were a gift from Dr. Masatoshi Takeichi. C57BL/6-Tg(*Cdh5-Cre*^{ERT2}) mice[66] were created by Dr. Yoshiaki Kubota and obtained from the CARD Mouse Bank (CARD ID: 2361, https://cardmice.com/rbase/changelang?lang=en) at Kumamoto University. For genetic loss-of-function studies, *Cdh5-Cre*^{ERT2} animals were crossed with *Cdh2*^{floxed} mice. Tamoxifen (Sigma-Aldrich, Cat# T5648) was dissolved in corn oil (Sigma-Aldrich, Cat# C8267) at 20 mg/mL and administered via maternal oral gavage from E16.5 to E18.5. Tamoxifen-administered *Cdh2*^{floxed} littermates were used as controls.

Animals were housed in cages lined with chip bedding in a controlled environment (23 ± 1°C, 12-h light/dark cycle starting at 08:00). Food and water were provided *ad libitum*. Timed pregnancies were established by placing male and female mice together overnight; the presence of a vaginal plug the following morning was designated as E0.5. The day of birth was defined as postnatal day (P)0. Pups were classified as 0 h after birth when birth was witnessed, and they were decapitated immediately thereafter (at P0, 0 h). Both male and female mice were used in all experiments. All procedures involving live animals were performed in accordance with the guidelines and regulations of Nagoya City University, Aichi, Japan.

Please cite this article in press as: Takemura et al., Transformation of radial glia into postnatal neural stem cells depends on birth, Cell Reports (2025), https://doi.org/10.1016/j.celrep.2025.116029

CellPress
OPEN ACCESS

Human specimens

We reanalyzed the dorsal-lateral part of the V-SVZ from three term (gestational ages $\geq$ 37 weeks) and three preterm (gestational ages $\leq$ 34 weeks) human tissue specimens used in our previous study.[10] Corrected gestational age at death was from 41 to 54 weeks. Only brains with unremarkable neuropathological findings were included; cases with major congenital anomalies or established genetic diagnoses were excluded. All fixed tissue specimens were acquired from NIH Neurobiobank. All methods were performed in accordance with the guidelines and regulations of Children's National Hospital and Children's National Research Institute, Washington DC, USA.

METHOD DETAILS

Mifepristone-induced preterm birth

Mifepristone treatment was performed as previously described, with modifications.[67,68] Mifepristone is an antagonist of progesterone and glucocorticoid receptors.[69] Mifepristone (RU-486; Sigma-Aldrich, Cat# M8046; 0.15mg/mL) was dissolved in 1.5% ethanol in MilliQ water and administered subcutaneously at E17.5 to induce delivery at E18.5 (preterm birth) or E19.5 (term birth). As reported previously,[68] these preterm birth mice showed no differences in offspring number or weight compared to term birth mice.

Cesarean section-induced preterm birth

Cesarean section was performed as previously described, with modifications.[70] Pregnant mice were anesthetized with isoflurane (Viatris), and pups were immediately extracted from the uterus. The umbilical cords were cut, and pups were removed from the amniotic membranes and massaged until spontaneous breathing was observed.

Progesterone-induced prolonged gestation

Pregnancy was prolonged by administering exogenous progesterone as previously described.[71] Medroxyprogesterone 17-acetate (Sigma-Aldrich, Cat# M1629; 16 mg/kg in 0.4 mL sterile saline) was diluted in sterile saline and injected daily subcutaneously to pregnant mice from E15.5 to E18.5.

In utero surgeries

In utero electroporation was performed as described previously.[72] Briefly, E17.5 timed-pregnant mice were anesthetized with isofluorane, and their uterine horns were exposed via midline laparotomy. Two microliters of a pCAGGS-EmGFP-miR-LacZ mixture were manually injected into the lateral ventricles of E17.5 embryonic brains. Five consecutive square-wave pulses (50 V, 50 ms duration) were applied to each embryo using an electroporator (NEPA21, NepaGene). The uterine horns were then returned to the abdominal cavity.

Viral vectors and plasmids and *in vivo* viral infection

Lentiviral vectors (CSII-based, provided by Dr. Hiroyuki Miyoshi, RIKEN Tsukuba BioResource Center) were generated as described previously.[55] The targeted sequences for mouse Cltc and Cdh2 genes were inserted into a modified Block-iT Pol II miR RNAi entry vector containing EmGFP (Thermofisher, K493500). A lacZ target sequence was used as a control, as described previously.[55] A CAAX box was added to localize fluorescent proteins to the plasma membrane by inverse PCR. The Gateway system (pENTR™/D-TOPO™ Cloning Kit, Thermofisher, K240020SP; Gateway™ LR Clonase™ II Enzyme mix, Thermofisher, 11791100) was used to generate CSII-EF-EmGFP-CAAX-miR-LacZ, CSII-EF-EmGFP-CAAX-miR-Cltc, CSII-EF-EmGFP-CAAX-miR-Cdh2, and CSII-hGFAP-tdTomato-CAAX. hGFAP was cloned by hGFAP-Cre (Addgene, Plasmid #40591). These viral vectors and packaging vectors (pCAG-HIVgp: RIKEN Bio Resource Center, RDB04394; pCMV-VSV-G-RSV-Rev: RIKEN Bio Resource Center, RDB04393) were co-transfected into HEK293T cells to produce lentiviral particles, and culture supernatants were collected and concentrated by centrifugation at 8,000 rpm for 16 h at 4°C.

For Cltc- and Ncad-KD experiments, pregnant mice were anesthetized with isoflurane at E16.5. After laparotomy, the uterus of the pregnant animal was exposed and 2 μL of lentiviral suspension was injected manually into the lateral ventricles of embryo brains. The incision was closed with sutures. For CSII-hGFAP-tdTomato-CAAX injection, term birth mice at P0.5 and preterm mice at P1.5 were anesthetized by hypothermia (4 min) and fixed in a stereotaxic injection apparatus (David Kopf Instruments). Two microliters of lentivirus were injected bilaterally into the lateral ventricles (coordinates: 1.5 mm anterior, 0.8 mm lateral to lambda, and 2.5 mm deep).

Brain slices live imaging

Brain slice imaging was performed as previously described, with modifications.[55] pCAGGS-EGFP-miRLacZ was electroporated into E17.5 ICR mice. At E18.5, 300-μm-thick coronal brain slices were prepared using a vibratome and placed on 0.4 mm Millicell inserts (Millipore, PICM0RG50) in 35 mm glass-bottom dishes (Nunc, 150680) containing imaging medium. Slices were cultured in Neurobasal medium (Gibco) supplemented with 10% fetal bovine serum, 2% MACS NeuroBrew-21 (Miltenyi Biotec), 1% Glutamax (Gibco), and 1% Antibiotic-Antimycotic (Gibco) in a 37°C stage-top chamber with 5% CO_2 (Tokai Hit).

To reduce oxygen levels, tissue slices were set into a sealed airtight container containing an AnaeroPack Bikouki (pO_2: 6–12%; pCO_2: 5–8%; A-28; Mitsubishi Gas Chemical Company) and incubated at 37°C for 6 hours. To determine the effect of calpain

Please cite this article in press as: Takemura et al., Transformation of radial glia into postnatal neural stem cells depends on birth, Cell Reports (2025), https://doi.org/10.1016/j.celrep.2025.116029

inhibitors on transection of RG fibers, brain slices were cultured on a filter membrane with 30 μM Calpain inhibitor III (Bachem) at 37°C for 6 h. To determine the effect of endocytosis inhibitors on transection of RG fibers, brain slices were cultured on a filter membrane with 30 μM MiTMAB (Sigma-Aldrich) at 37°C for 6 h. The cultured slices were then fixed with 4% paraformaldehyde (PFA) in 0.1 M phosphate buffer (PB) (pH 7.4) and subjected to immunohistochemistry using an anti-GFP antibody (1:200, Medical & Biological Laboratories). Time-lapse images were captured at 5-min intervals using an LSM880 laser-scanning confocal microscope with a 10× dry objective lens (Carl Zeiss), and figures and videos were prepared using ZEN (Carl Zeiss).

Immunohistochemistry, confocal image acquisition and quantification

For mouse tissue, immunohistochemistry was performed as described previously.[56] Briefly, embryos and neonates were decapitated, and adult mice were transcardially perfused with PBS followed by 4% PFA in 0.1 M PB. In all cases, brains were removed and postfixed in the same fixative overnight at 4°C. Floating 60-μm-thick coronal sections were prepared using a vibratome. For quantitative analysis, every sixth 60-μm-thick section was obtained. Sections matched to bregma were incubated for 40 min in blocking buffer [10% normal donkey serum (Millipore), 2% unlabeled goat Fab against mouse IgG (Jackson ImmunoResearch Laboratories), and 0.4% Triton X-100 in PBS], then overnight at 4°C with primary antibodies, followed by 2 h incubation with Alexa Fluor-conjugated secondary antibodies (1:500; Invitrogen). The following primary antibodies were used: chicken IgG against glial fibrillary acidic protein (GFAP) (1:1,000; Abcam), against nestin (1: 2,000; Aves Labs), against RFP (1:2,000; Rockland); mouse IgG against Mash1 (1:1,000; Santa Cruz Biotechnology, Dallas), against N-cadherin (1:500, BD Biosciences), against α-Actin (1:500; Santa Cruz Biotechnology); rat IgG against GFP (1:500; Nacalai Tesque); rabbit IgG against GFP (1:500; Medical & Biological Laboratories), anti-DsRed (1:200, Takara), against Mfsd2a (1:500, Cell Signaling Technology), against N-cadherin (1:200, Abcam, ab12221), against EGFR (1:100; Santa Cruz Biotechnology); and Armenian hamster IgG against CD31 (clone 2H8, DSHB; dilution 1:20). For nuclear staining, Hoechst 33342 (1:3,000; Thermo Fisher Scientific) was used. Labeled sections were mounted on glass slides, and coverslips were sealed with Vectashield (Vector Laboratories). To visualize RG in a hemisphere, floating 300-μm-thick coronal sections were prepared using a vibratome. These were stained using the same protocol with rabbit anti-GFP (1:500) as the primary antibody. Imaging was performed with an FV3000 confocal microscope using a 20× dry objective (Evident). Tile scans of the dorsal-lateral V-SVZ were acquired with z-stacks covering visible tissue. Z-step size was 0.9–0.96 μm.

In *GFAP-EGFP* mice, $EGFP^+$ cells with apical contacts at the lateral ventricle were classified as postnatal NSCs. For the analyses of $EGFP^+GFAP^+$ NSCs, $EGFP^+EGFR^+Mash1^+$ cells, and $EGFR^+Mash1^+$ intermediate progenitor cells, immunopositive cells were counted, and densities were calculated. Fluorescence intensity of $N\text{-cadherin}^+$ signals in RG and vascular indices[73] were quantified using FIJI (National Institutes of Health). Relative vessel lengths were quantified using CellSens (Evident). Z-stack images of RG and NSCs were traced and analyzed with Neurolucida software (MBF Bioscience). Cells with truncated fibers due to sectioning were excluded from analysis. We excluded from our analysis the cells whose fibers were cut off by preparing coronal sections. Therefore, there is a possibility that the average fiber length we estimated was shorter than the actual average fiber length, especially in groups with long fiber lengths.

For human tissue, cryoprotected blocks were cut into 20-μm-thick coronal sections using a cryostat. Antigen retrieval was performed with 10 mM sodium citrate buffer (pH 6.0) at 95°C for 10 min. Sections were washed with 0.2% Triton-X in PBS, incubated in 3% H_2O_2 in 0.2% Triton X-100 in PBS for 45 min at RT, and then blocked in TNB buffer [0.5% blocking reagent (Akoya Biosciences, FP1012) in 0.1 M Tris-HCl, pH 7.6] for 1 h at RT. Sections were incubated with primary antibodies in TNB overnight at 4°C, then with biotinylated or Alexa Fluor-conjugated secondary antibodies for 2 h at RT. Streptavidin-horseradish peroxidase was applied for 30 min, followed by TSA amplification (1:500) for 5 min at RT. Sections were washed with 0.3% Triton-X in 0.1 M PBS and mounted with VECTASHIELD with DAPI (Vector Laboratories). As a primary antibody, rabbit IgG against doublecortin (Dcx) (1:200; Cell Signaling Technology) and chicken IgY against Vimentin (1:500; Millipore) were used. Images were acquired using an FV1000 confocal microscope with a 10× or 20× dry objective lens (Evident). Individual tiles were stitched using FIJI.

Western blotting

Western blotting was performed as described previously.[56] To confirm the efficiency of KD by the Cltc miRNA, Neuro2A cells were transfected with plasmids expressing CSII-EF-EmGFP-CAAX-miR-Cltc or CSII-EF-EmGFP-CAAX-miR-LacZ for control. After 96 h, cells were collected and lysed in lysis buffer [50 mM Tris-HCl (pH 8.0), 150 mM NaCl, 1% NP-40, 0.5% sodium deoxycholate, 0.1% sodium dodecyl sulfate (SDS), protease inhibitor cocktail (Nacalai Tesque, 03969-21)] using ultrasound sonication. Protein concentration was measured using a Bio-Rad Protein Assay Dye Reagent Concentrate (Bio-Rad, Cat# 500-0006) and adjusted. Proteins were separated by SDS-polyacrylamide gel electrophoresis and transferred to PVDF membranes (Millipore, Cat# IPVH00010). Membranes were blocked in 2% skim milk (Wako, Cat# 190-12865) in Tris-buffered saline (TBS) containing 0.1% Tween-20 for 40 min, incubated with primary antibodies overnight at 4°C, and then with horseradish peroxidase-conjugated secondary antibodies (Jackson ImmunoResearch) for 1 h. Signals were detected with ECL Prime Western Blotting System (Cytiva, RPN2232) and visualized with an ImageQuant LAS 4000 mini (GE Healthcare). Semi-quantitative analysis was performed using FIJI. The following primary antibodies were used: mouse IgG against Cltc antibody (1:200; Santa Cruz) and against β-actin antibody (1:10,000; Sigma-Aldrich).

Please cite this article in press as: Takemura et al., Transformation of radial glia into postnatal neural stem cells depends on birth, Cell Reports (2025), https://doi.org/10.1016/j.celrep.2025.116029

SBF-SEM

SBF-SEM analyses were performed as described previously with slight modifications.[74–78] P0 (0 h and 6 h after birth) mouse brains were fixed by transcardiac perfusion with 2.5% glutaraldehyde and periodate-lysine-paraformaldehyde (PLP: 2% paraformaldehyde containing 0.074 M lysine and 0.01 M sodium periodate) in 0.04 M PB (pH 7.4) at 4°C, followed by postfixation in the same fixative for 20 h at 4°C. Term P28.5 and preterm P29.5 mouse brains were fixed by transcardiac perfusion with 2.5% glutaraldehyde and 2% PFA in 0.1 M PB (pH 7.4) at 4°C and postfixed in the same fixative for 2 days at 4°C. Coronal sections (300 μm thick) were prepared using a vibratome, and dorsal-lateral parts V-SVZ regions were dissected using an ophthalmic knife under a stereomicroscope. These tissue blocks were treated sequentially with 2% OsO_4 and 1.5% potassium ferricyanide in PBS for 1 h at 4°C, 1% thiocarbohydrazide for 20 min at room temperature (RT), 2% aqueous OsO_4 for 30 min at RT, uranyl acetate overnight at 4°C, and lead aspartate for 2 h at 50°C. Tissues were dehydrated in a graded ethanol series and treated with dehydrated acetone. Coronal V-SVZ sections (1 mm × 1 mm × 300 μm) were embedded in Durcupan resin containing 8% Ketjen black powder for two days at 60°C. SBF-SEM imaging was performed using a Merlin or SigmaVP scanning electron microscope (Carl Zeiss) equipped with a 3View in-chamber ultramicrotome system (Gatan). Serial images were acquired at 6.625 nm/pixel with 50 nm steps (P0) or 6.0 nm/pixel with 80 nm steps (Term and Preterm adults). Sequential images were processed using FIJI software. Cells were identified based on the ultrastructural features as previously reported.[21] NSCs were defined as cells with a single primary cilium facing the ventricular surface, and ependymal cells as those with multiple cilia. Segmentation was performed using Volume Annotation and Segmentation Tool *Lite* (for P0 samples; https://lichtman.rc.fas.harvard.edu/vast/)[60] and Microscopy Image Browser (for Term P28.5 and Preterm P29.5 samples; https://mib.helsinki.fi/).[61] For 3D reconstruction, analysis of cell-to-cell adhesion surface, and printable model generation, Amira software (Thermo Fisher, 6.2.0, 2020.2) was used. Blender (https://www.blender.org) and Sketchfab (https://sketchfab.com) were used to prepare interactive 3D models.

Single-cell isolation

The V-SVZ tissues of C57BL6/J mice were dissected for scRNA-seq, as described previously.[79] Bilateral V-SVZ tissues dissected from three littermates were pooled for one sample. Two independent biological replicates were prepared per timepoint (term P28.5: P28.5-1 and P28.5-2; preterm P29.5: P29.5-1 and P29.5-2). Tissues were digested for 60 min at 37°C with Papain-EBSS (LK003150; Worthington), with mechanical dissociation using pipettes every 10 min. Cell suspensions were filtered through 70-μm and 40-μm strainers (Corning), centrifuged for 5 min at 300 g at room temperature, and resuspended with DNase solution containing ovomucoid inhibitor. After further centrifugation, cells were suspended in RNase-free PBS (Invitrogen) with 0.04% ultrapure bovine serum albumin and 0.1 U/mL recombinant RNase inhibitor (Thermofishe) at 1,000 cells/μL. Trypan blue (Thermo Fisher) confirmed >90% viability.

10× Genomics single-cell library preparation

A suspension of 10,000 single cells was loaded onto a Chromium Next GEM Chip G (PN-2000177; 10× Genomics). cDNA synthesis and library construction were performed according to the Chromium Single Cell 3′ v3.1 protocol (PN-1000128; 10× Genomics). Samples P28.5-1 and P29.5-1 were processed on one chip, and P28.5-2 and P29.5-2 on another. Sequencing was performed using the NovaSeq 6000 platform (Illumina), generating 150 bp paired-end reads.

Analysis of scRNA-seq data

Primary data analysis was performed using Cell Ranger v5.0.0 (10× Genomics) to generate fastq files (cellranger mkfastq) and count matrices (cellranger count). The mouse reference transcriptome used by cellranger count was downloaded from 10× Genomics (https://cf.10xgenomics.com/supp/cell-exp/refdata-gex-mm10-2020-A.tar.gz). Secondary analysis was carried out on the filtered feature barcode matrices.

Cell filtering

Cell filtering was performed using the R package CRMetrics v0.2.3.[62] This package bundles typical preprocessing steps and provides visual assessment of filtered cells. Scrublet[63] was used to determine doublet scores for each cell, and only cells below the sample-specific threshold were included in downstream analysis. In addition, cells with a mitochondrial gene fraction > 7% and cells with a Unique Molecular Identifier (UMI) count < 750 were eliminated.

Sample integration and clustering

Pagoda2 (https://github.com/kharchenkolab/pagoda2) was used to normalize each of the datasets (min.cells.per.gene = 3). Subsequently, term P28.5 and preterm P29.5 samples were integrated using Conos[64] (https://github.com/kharchenkolab/conos). To ensure better alignment of the samples, the alignment.strength parameter was set to 0.3. UMAP embedding was estimated and clustering was performed using the method leiden.community. To increase the resolution of the clustering, the resolution parameter was set to 5 and min.group.size to 15. The final clusters were generated using a combination of manual selection and findSubcommunities function of Conos to split the clusters further. The clusters were annotated using known cell-type-specific marker genes from the literature.

Please cite this article in press as: Takemura et al., Transformation of radial glia into postnatal neural stem cells depends on birth, Cell Reports (2025), https://doi.org/10.1016/j.celrep.2025.116029

For subclustering of RG, the clusters named ''Radial glia'', ''Mki67$^+$ RG'' and ''Intermediate progenitor cells'' were extracted from the E18.5 and preterm P0.5 dataset of our previous paper.[10] After initial integration, embedding and clustering of the samples, one cluster containing undefined cells and immature projection neurons was removed. For the final integration, Conos' alignment. strength parameter was set to 0.3. UMAP embedding and clustering were estimated using Conos. The clusters were annotated using known cell-type-specific marker genes from the literature.

Expression of cell adhesion related genes

The normalized joint count matrix was extracted from the Conos object and cells corresponding to RG and endothelial/pericyte/vascular smooth muscle cell clusters in term P2.5 samples were selected. Genes were filtered based on the GO term "cell adhesion" (GO:0007155), and mean expression per cell type was computed. Genes with zero expression in both cell types were removed. The results can be found in Table S1, sheet2.

Differential gene expression analysis

Cacoa (https://github.com/kharchenkolab/cacoa)[65,80] was used for DEG analysis. Cacoa's function estimateDEPerCellType with the default parameters was applied to estimate genes differentially expressed between the two different conditions per cell type. This function is based on the DESeq2 package and collapses the gene expression per sample and per cell type into pseudo-bulk gene expression levels. DESeq2 uses the Wald test to estimate DEGs. The results for the cell adhesion-related genes in RG and endothelial cell/pericyte/vascular smooth muscle cell clusters of E18.5 and term P2.5 samples can be found in Table S1, sheet 3,4, and those of term P2.5 and preterm P3.5 samples can be found in Table S1, sheet 8,9.

Gene set enrichment analysis

First, differentially expressed genes between conditions per cell type were estimated using Cacoa's[65,80] function estimateDEPerCellType. Then, GSEA was performed using Cacoa's function estimateOntology with the default settings. This function is based on the package clusterProfiler.[81] The results for the astrocyte and endothelial cell clusters at term P28.5 and preterm P29.5 can be found in Table S1, sheet 6,7. The results for the RG_3 subcluster at E18 and preterm P0 can be found in Table S1, sheet 1. The dot plots for specific GO terms were generated using the dotplot function from the package enrichplot.[82] Heatmaps showing the top 30 down- or upregulated collapsed GO terms were generated using the function plotOntologyHeatmapCollapsed on the Cacoa object. Only GO terms from the category ''biological process'' were included. The words ''cell,'' ''regulation,'' and ''process'' were excluded from the collapsed GO terms.

QUANTIFICATION AND STATISTICAL ANALYSIS

All images were analyzed with the experimenter blinded to treatment groups. Sample sizes were not predetermined but were chosen based on previous studies.

Statistical significance was assessed using unpaired Welch's t-test. For comparisons among three independent groups, one-way ANOVA followed by Tukey's multiple comparison test was used. Fisher's exact test was applied to quantify endfoot-possessing RG/postnatal NSCs. Statistical significance was defined as $^*p < 0.05$, $^{**}p < 0.01$, and $^{***}p < 0.001$. Error bars represent the standard error of the mean (SEM). These statistical analyses were conducted using GraphPad Prism 10 (GraphPad Software). For GSEA, dot size reflects the number of genes and color represents the adjusted *p*-value (Benjamini–Hochberg adjustment).

Cell Reports, Volume ■ ■

Supplemental information

Transformation of radial glia into postnatal neural stem cells depends on birth

Shoko Takemura, Koya Kawase, Laura Wolbeck, Yasuhisa Nakamura, Mami Matsumoto, Hideo Jinnou, Aika Tahara, Masato Sawada, Yoshiaki Kubota, Vicente Herranz-Pérez, José Manuel García-Verdugo, Nobuyuki Ishibashi, Vittorio Gallo, Nobuhiko Ohno, Konstantin Khodosevich, and Kazunobu Sawamoto

Supplementary information

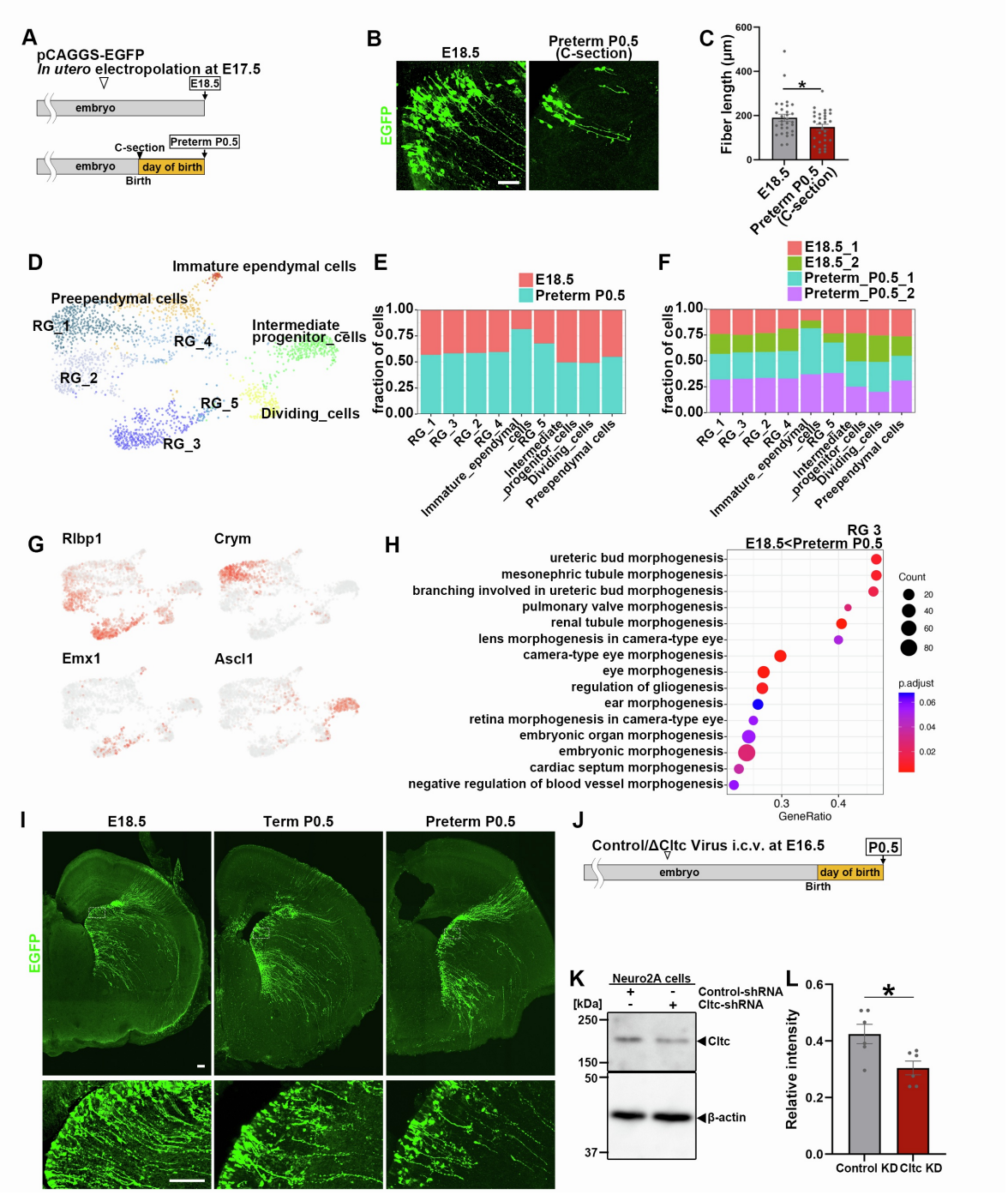


Figure S1: Morphology and GSEA analysis of RG around birth, Related to Figure 1.
(A) Experimental timeline. Cesarean section was performed to induce preterm birth. (B)

Representative images of EGFP$^+$ RG in the V-SVZ at E18.5 and preterm P0.5 induced by cesarean section. (C) Quantification of RG fiber length in the V-SVZ at E18.5 and preterm P0.5 induced by cesarean section. (D) UMAP representation of scRNA-seq data of RG, immature ependymal cells, preependymal cells, dividing cells and intermediate progenitor cells in the V-SVZ at E18.5 and preterm P0.5. (E) Proportion of cells per condition per cell type. (F) Proportion of cells per sample per cell type. (G) Expression of marker genes visualized on the UMAP embedding. *Rlbp1*, highly expressed in the dorsal region of the V-SVZ, especially in the dorsal-lateral region of the V-SVZ [25], was enriched in cluster RG 2, 3, 4, and 5. *Crym* is expressed in the ventral region of the V-SVZ. *Crym* was enriched in cluster RG 1. *Emx1*, localized in the dorsal and dorsal-lateral region of the V-SVZ [72], was enriched in cluster RG 3 and RG 5. *Ascl1*, a proneuronal transcription factor, was enriched in cluster RG 4, RG 5, Dividing cells and intermediate progenitor cells. (H) Dot plots of GSEA results showing selected GO terms in the RG 3 cluster. Gene ratio is the proportion of significant genes associated with the given GO term. Dot size indicates the number of genes, and the color shows adjusted *p*-value (Benjamini–Hochberg adjustment). (I) Representative images of RG in a 300-μm-thick coronal brain section at E18.5, Term P0.5, and Preterm P0.5. (J) Experimental timeline. Cltc-KD lentivirus was injected at E16.5. Morphological analysis of RG was performed at P0.5. (K) Western blots using an anti-Cltc antibody showed that the endogenous Cltc protein was efficiently reduced by Cltc-KD in Neuro2A cells. β-actin was used as a loading control. (L) Semi-quantification of the Cltc-KD. $^*p < 0.05$. Scale bars, 50 μm (B), 100 μm (I). Error bars, mean ± SEM.

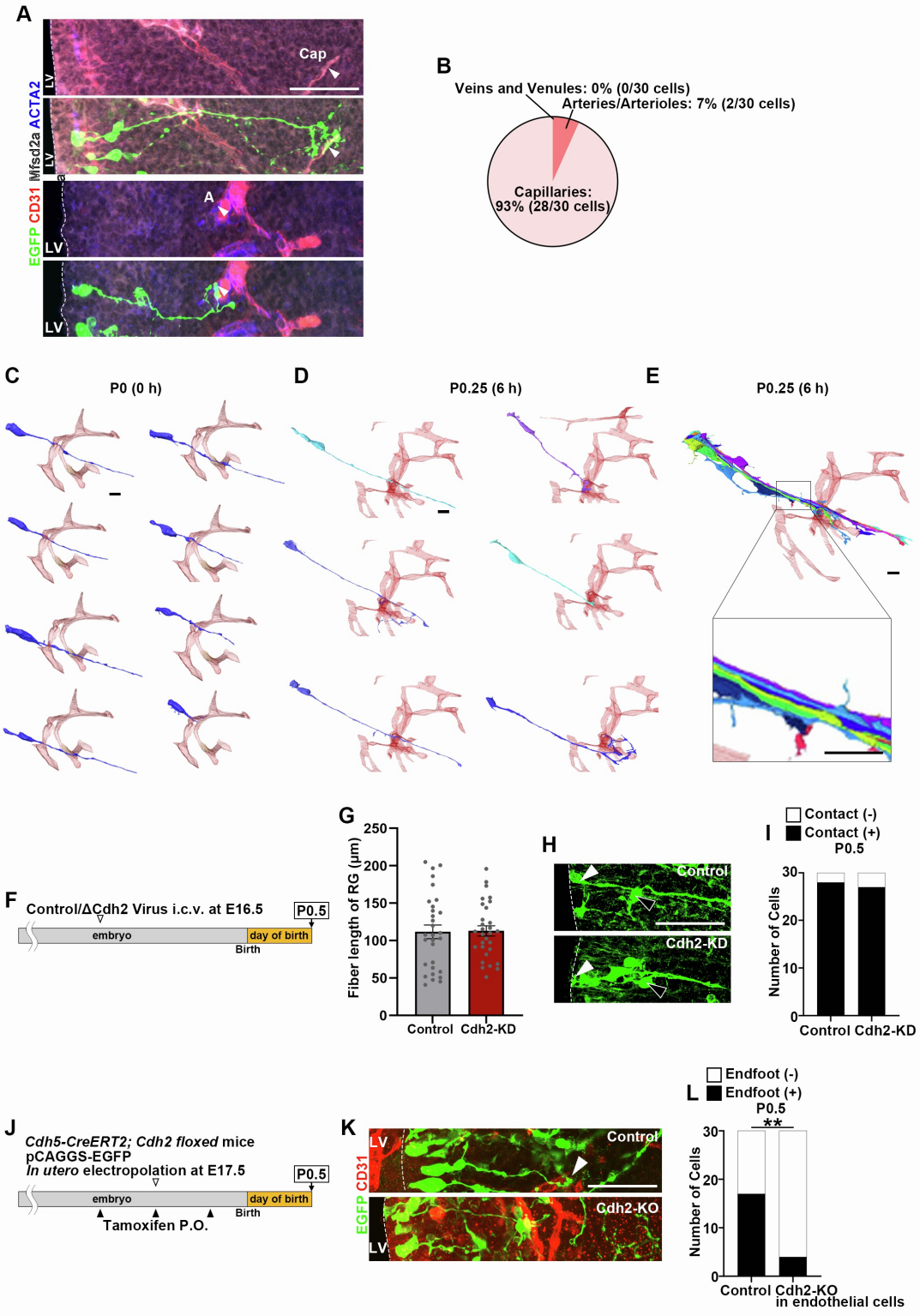

A
Cap
LV
Mfsd2a ACTA2
EGFP CD31
A
B
Veins and Venules: 0% (0/30 cells)
Arteries/Arterioles: 7% (2/30 cells)
Capillaries:
93% (28/30 cells)
C
P0 (0 h)
D
P0.25 (6 h)
E
P0.25 (6 h)
F
Control/ΔCdh2 Virus i.c.v. at E16.5
P0.5
embryo
day of birth
Birth
G
Fiber length of RG (μm)
250
200
150
100
50
0
Control
Cdh2-KD
H
Control
Cdh2-KD
I
Contact (-)
Contact (+)
P0.5
Number of Cells
30
20
10
0
Control
Cdh2-KD
J
Cdh5-CreERT2; Cdh2 floxed mice
pCAGGS-EGFP
In utero electropolation at E17.5
P0.5
embryo
day of birth
Birth
Tamoxifen P.O.
K
LV
CD31
EGFP
Control
Cdh2-KO
LV
L
Endfoot (-)
Endfoot (+)
P0.5
**
Number of Cells
30
20
10
0
Control
Cdh2-KO
in endothelial cells

Figure S2: Analysis of RG endfeet around birth, Related to Figure 2. (A) Representative images of RG each forms an endfoot (arrowheads) and vasculature in V-SVZ at term P0.25 (6 h). To distinguish the type of vessels, we used ACTA2 (smooth muscle actin) as an artery/arteriole marker, and Mfsd2a as a capillary marker, according to previous research [73]. (B) Quantification of specific vessel types in which each RG forms its endfoot in the V-SVZ at term P0 (6 h). (C-E) SBF-SEM analysis of P0 V-SVZ. At 0 h after birth, RG predominantly retained long fibers with partial contact at the mid-fiber region (C). At 6 h after birth, some RG retained long fibers with partial contact at the mid-fiber region, whereas the other displayed an enlarged endfoot in direct contact with endothelial cells (D). Some RG formed bundles at 6 h after birth (E). (F) Experimental timeline. (G) Quantification of RG fiber length in control and *Cdh2*-KD conditions at P0.5. (H) Representative images of RG that have (open arrowheads) and do not have (closed arrowhead) a contact with the ventricular surface in the control and *Cdh2*-KD conditions at P0.5. (I) Quantification of the effect of *Cdh2*-KD in RG on the contact with ventricular surface at P0.5. (J) Experimental timeline. (K) Representative images showing the effect of conditional knockout of *Cdh2* in endothelial cells using *Cdh5-Cre*^{ERT2}*; Cdh2*^{floxed} mice on an endfoot formation (arrowhead) in each RG-derived cell in the V-SVZ at P0.5. (L) Quantification of endfoot-forming RG-derived cells in control and N-cadherin-knockout conditions in endothelial cells at P0.5. $^{**}p < 0.01$. Scale bars, 10 μm (C-E), 50 μm (A, H, K). A, artery or arteriole; Cap, capillary. Error bars, mean ± SEM.

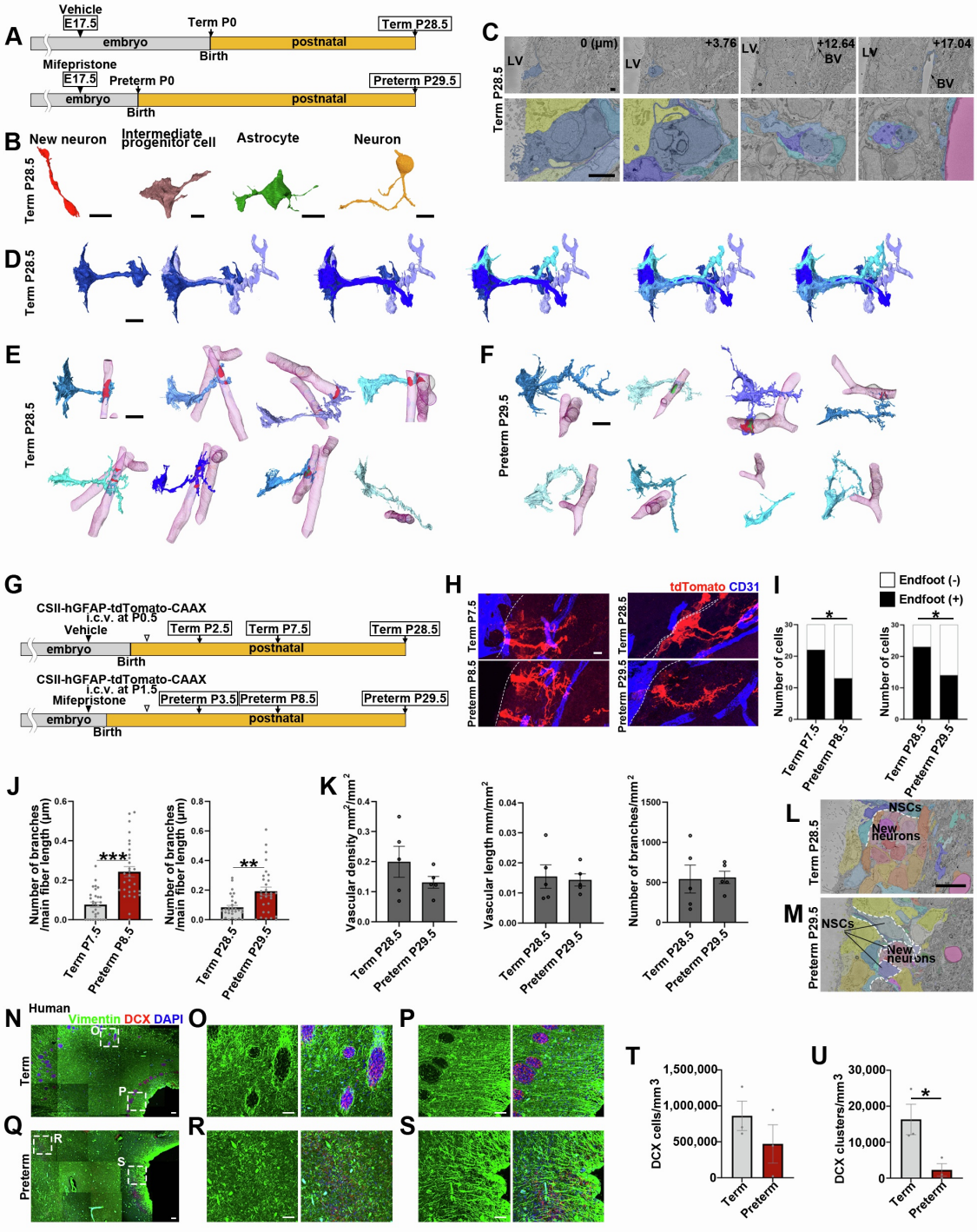

A
Vehicle
E17.5
Term P0
Term P28.5
embryo
postnatal
Birth
Mifepristone
E17.5
Preterm P0
Preterm P29.5
embryo
postnatal
Birth
B
New neuron
Intermediate progenitor cell
Astrocyte
Neuron
Term P28.5
C
Term P28.5
0 (μm)
+3.76
+12.64
+17.04
LV
BV
D
Term P28.5
E
Term P28.5
F
Preterm P29.5
G
CSII-hGFAP-tdTomato-CAAX
i.c.v. at P0.5
Vehicle
Term P2.5
Term P7.5
Term P28.5
embryo
postnatal
Birth
CSII-hGFAP-tdTomato-CAAX
i.c.v. at P1.5
Mifepristone
Preterm P3.5
Preterm P8.5
Preterm P29.5
embryo
postnatal
Birth
H
tdTomato CD31
Term P7.5
Preterm P8.5
Term P28.5
Preterm P29.5
I
Endfoot (-)
Endfoot (+)
Number of cells
Term P7.5
Preterm P8.5
Term P28.5
Preterm P29.5
J
Number of branches /main fiber length (μm)
***
**
Term P7.5
Preterm P8.5
Term P28.5
Preterm P29.5
K
Vascular density mm²/mm²
Vascular length mm/mm²
Number of branches/mm²
Term P28.5
Preterm P29.5
L
Term P28.5
NSCs
New neurons
M
Preterm P29.5
NSCs
New neurons
N
Human
Vimentin DCX DAPI
Term
Preterm
O
P
Q
R
S
T
DCX cells/mm3
1,500,000
1,000,000
500,000
0
Term
Preterm
U
DCX clusters/mm3
30,000
20,000
10,000
0
*
Term
Preterm

Figure S3: SBF-SEM analysis of young adult term and preterm V-SVZ, and analysis of NSCs and their role as tunnels for new neurons in the mouse and human V-SVZ, related to Figures 3 and 4. (A) Experimental timeline. Mifepristone administration was performed to induce preterm birth at E17.5. SBF-SEM experiment was performed at term P28.5 and preterm P29.5. (B) The 3D morphology of each cell. (C) 2D images of an NSC with neighboring cells. (D) The fibers of inner NSCs were surrounded by fibers of outer NSCs in a layered structure in the V-SVZ at term P28.5. (E) NSCs, endothelial cells and pericytes of term P28.5 V-SVZ. Directly adhered area of NSC endfoot and vascular endothelial cells are shown in red and directly adhered area of NSC endfoot and pericytes are shown in green. (F) NSCs (blue series), endothelial cells (semi-transparent pink) and pericytes (semi-transparent white) of preterm P29.5 V-SVZ. Directly adhered area of NSC endfoot and vascular endothelial cells are shown in red and directly adhered area of NSC endfoot and pericytes are shown in green. (G) Experimental timeline. Mifepristone administration was performed to induce preterm birth at E17.5. CSII-hGFAP-tdTomato-CAAX lentivirus was injected at term P0.5/preterm P1.5 to visualize the postnatal NSCs. Morphological analysis of postnatal NSCs was performed at term P2.5/preterm P3.5, term P7.5/preterm P8.5, and term P28.5/preterm P29.5. (H) Representative images of the V-SVZ at term P7.5/preterm P8.5 and term P28.5/preterm P29.5. (I) Quantification of endfoot-possessing postnatal NSCs in the V-SVZ at term P7.5/preterm P8.5 and term P28.5/preterm P29.5. (J) Quantitative data of the number of branches per main fiber length of NSCs in the V-SVZ at term P7.5/preterm P8.5 and term P28.5/preterm P29.5. (K) Quantification of vascular density, length and branch number in the V-SVZ at term P28.5 and preterm P29.5. (L and M) 2D-SEM images of showing new neurons and the tunnel made by NSCs in the V-SVZ at term P28.5 (L) and preterm P29.5 (M). (N) Representative images of coronal V-SVZ sections of the term human brain stained for Vimentin (green) and Dcx (red). Nuclei were stained with DAPI (blue). (O and P) Magnified view of the boxed areas in (N). (Q) Representative images of coronal V-SVZ sections of the term human brain stained for Vimentin (green) and Dcx (red). Nuclei were stained with DAPI (blue). (R and S) Magnified view of the boxed areas in (Q). (T) Density of Dcx^+ cells in the human V-SVZ (n = 3 each; unpaired t-test). (U) Density of Dcx^+ clusters in the human V-SVZ (n = 3 each; unpaired t-test). *$p < 0.05$, **$p < 0.01$ and ***$p < 0.001$. Scale bars, 5 μm (C), 10 μm (B, D, E, F, H, and L), 50 μm (N, O, P, Q, R, and S). Error bars, mean ± SEM.

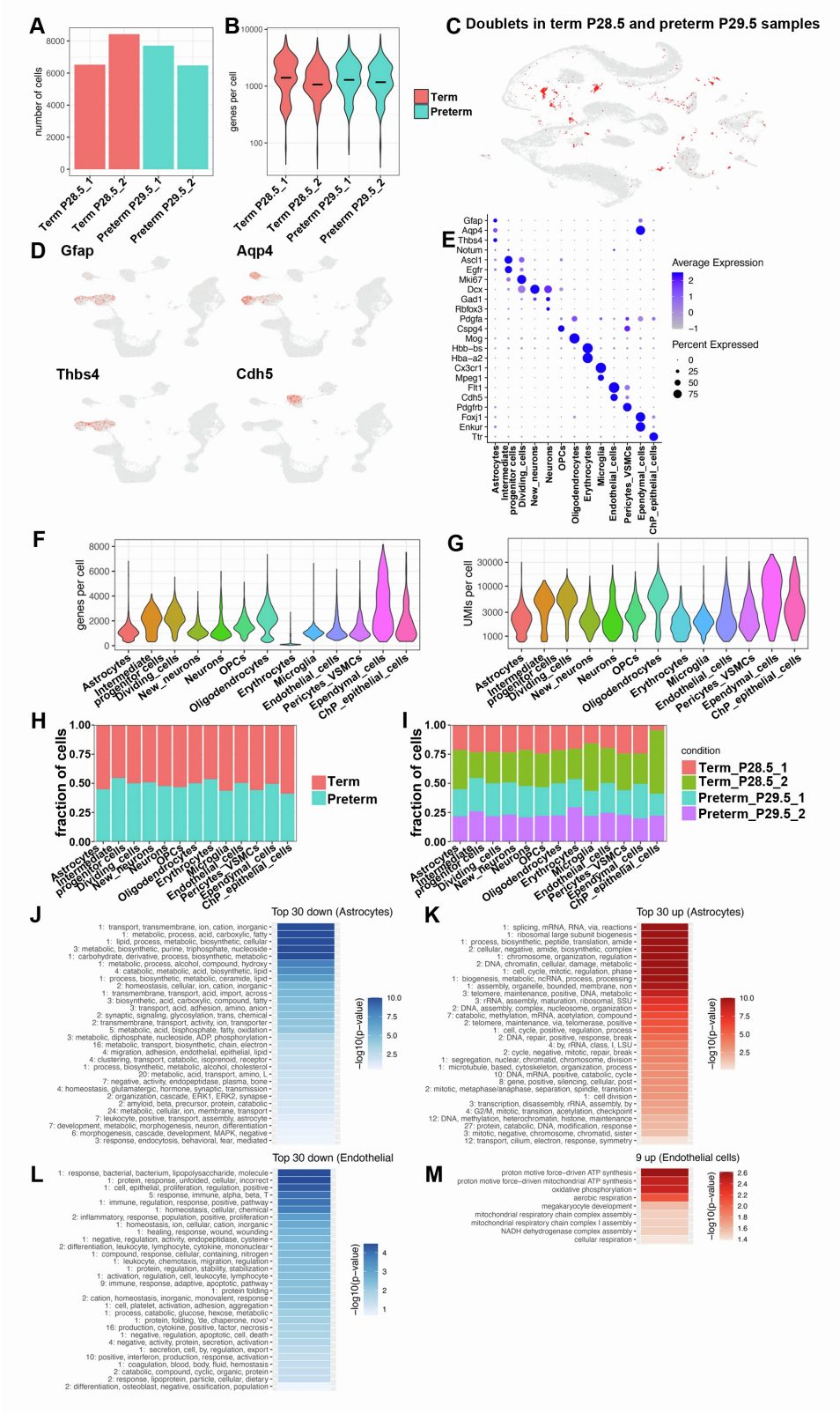

A
number of cells
Term P28.5_1
Term P28.5_2
Preterm P29.5_1
Preterm P29.5_2
B
genes per cell
C Doublets in term P28.5 and preterm P29.5 samples
Term
Preterm
D Gfap
Aqp4
Thbs4
Cdh5
E
Average Expression
Percent Expressed
F
genes per cell
G
UMIs per cell
H
fraction of cells
Term
Preterm
I
fraction of cells
condition
Term_P28.5_1
Term_P28.5_2
Preterm_P29.5_1
Preterm_P29.5_2
J Top 30 down (Astrocytes)
−log10(p−value)
K Top 30 up (Astrocytes)
L Top 30 down (Endothelial
M 9 up (Endothelial cells)

Figure S4: Characterization of scRNA-seq data, related to Figure 4.

(A) Number of sequenced cells per sample before filtering for low-quality cells. In total, 29,127 cells (term P28.5_1: 6,523 cells, term P28.5_2: 8,423 cells, preterm P29.5_1: 7,706 cells, preterm P29.5_2: 6,475 cells) were sequenced for term P28.5 and preterm P29.5. (B) Number of genes per cell detected for each sample. Black line represents the median. A median of 1,345 genes were detected per cell. (C) UMAP representation of term P28.5 and preterm P29.5 samples with excluded doublets marked in red. (D) Expression of marker genes visualized on the UMAP embedding. *Gfap*, *Aqp4*, and *Thbs4* gene expression was enriched in astrocytes cluster. Cdh5 gene expression was enriched in endothelial cells cluster. (E) Dot plot of marker gene expression of assigned cell types. (F) Number of genes per cell for each cell type. (G) Number of UMIs per cell for each cell type. (H) Proportion of cells per condition per cell type. (I) Proportion of cells per sample per cell type. (J) Top 30 downregulated GO terms in astrocytes of Preterm P29.5 compared with Term P28.5. The row labels show the number of GO terms, followed by the five most frequent words of the collapsed GO terms. (K) Top 30 upregulated GO terms in astrocytes of Preterm P29.5 compared with Term P28.5. (L) Top 30 downregulated GO terms in endothelial cells of Preterm P29.5 compared with Term P28.5. (M) All upregulated GO terms in endothelial cells of Preterm P29.5 compared with Term P28.5. The full list of significant GO terms can be found in Table S1, sheet 6 and 7.

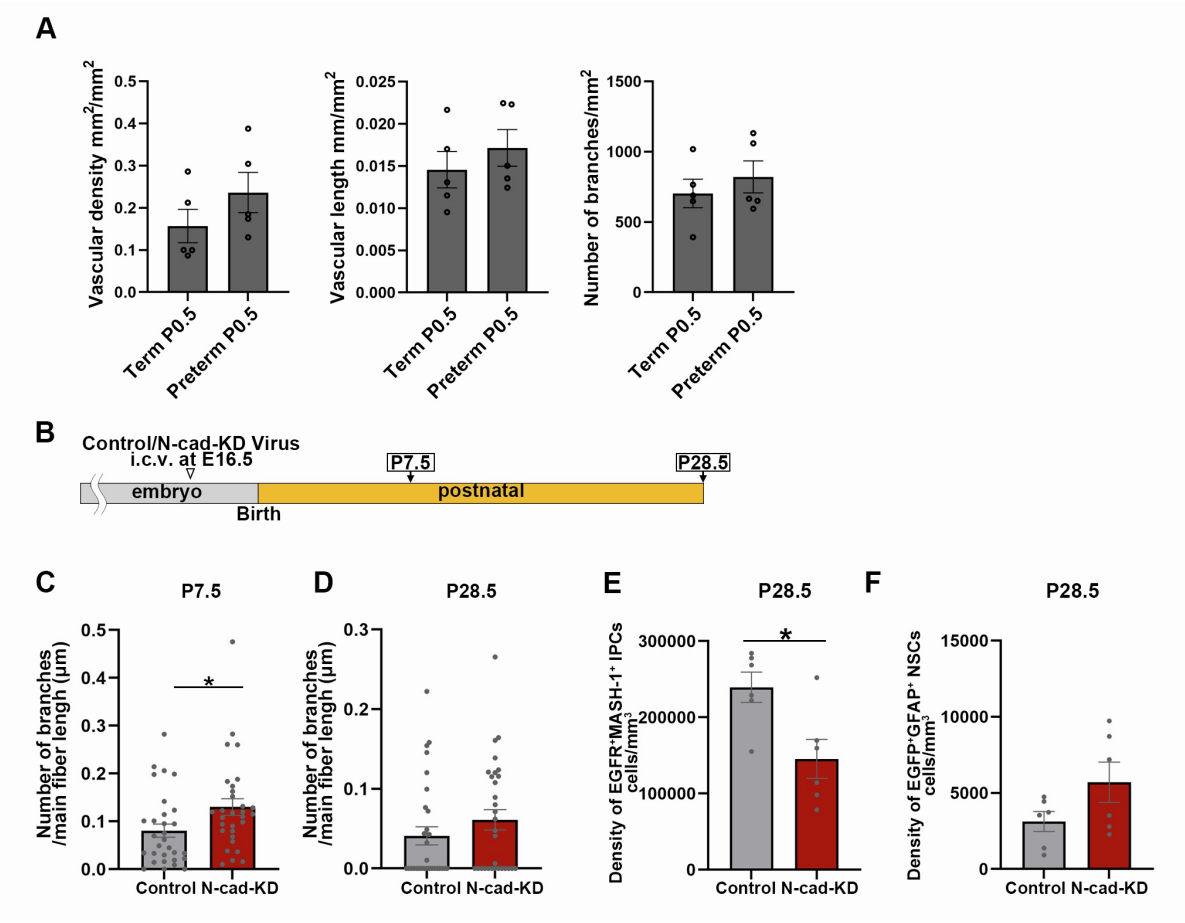


Figure S5: Effect of N-cadherin-KD on the morphology and stemness of young adult NSCs, related to Figure 5.

(A) Quantification of vascular density, length and branch number in the V-SVZ at term P0.5 and preterm P0.5. (B) Experimental timeline. N-cad-KD lentivirus was injected at E16.5. Morphological analysis of RG was performed at term P7.5 and P28.5. (C and D) Quantitative data of the number of branches per main fiber length of NSCs in the V-SVZ at term P7.5 (C) and P28.5 (D). (E) Quantification of the density of $EGFP^{+}Mash\text{-}1^{+}$ intermediate progenitor cells in the V-SVZ at term P28.5. (F) Quantification of the density of $EGFP^{+}GFAP^{+}$ NSCs in the V-SVZ at term P28.5. $^{*}p < 0.05$. Error bars, mean ± SEM.